Chapter 8
Mössbauer Spectroscopy in External Magnetic Fields

Michael Reissner

Abstract The application of external magnetic fields allows to broaden the knowledge, which can be gained by Mössbauer spectroscopy enormously. In combination with magnetic measurements, detailed information about local magnetic and electronic structure can be obtained. After an introduction to the influence of an external magnetic field on hyperfine interactions, examples are given. Starting from simple magnetic structures like para-, ferro-, and antiferro-magnetic ones, investigations on complex magnetic structures with spin canting are discussed. Also results on materials with inhomogeneous magnetic structures like spin glasses will be presented. Special focus will be on the influence of high external fields on the spin dynamics.

8.1 Introduction

In contrast to magnetization measurements or NMR investigations the application of an external field is not a prerequisite to get information about the magnetic behaviour of a compound in case of Mössbauer spectroscopy. Nevertheless measurements in external magnetic fields have been performed since the very early days of Mössbauer spectroscopy, because a lot of new and more in-depth information can be gained. Especially in the case of the investigation of magnetic ground state properties in-field measurements are extremely valuable. The determination of the precise hyperfine structure in magnetically ordered samples is often a non-trivial task. The simultaneous presence of magnetic dipole and electric quadrupole interaction makes modelling of the hyperfine structure quite complicate. But if external field is high the influence of electric field gradient can be reduced and interpretation of measured spectra might become easier. One of the first applications of external fields in Mössbauer spectroscopy was the measurements of the sign of the hyperfine field in α-Fe [1, 2]. For alloys with traces of iron the local susceptibility of the iron moments could be determined [3–7]. Knowledge about crystal field parameters and the atomic arrangement in complex structures, as well as the investigation of magnetic order can

M. Reissner (✉)
Institute of Solid State Physics, TU Wien, Vienna, Austria
e-mail: reissner@tuwien.ac.at

Y. Yoshida and G. Langouche (eds.), *Modern Mössbauer Spectroscopy*,
Topics in Applied Physics 137, https://doi.org/10.1007/978-981-15-9422-9_8

be obtained by high field Mössbauer spectroscopy [8, 9]. Tuning the field strength in such way that the magnetic and electrostatic hyperfine interaction is of similar strength, the sign of the electric field gradient can be obtained for 3/2 → 1/2 transitions, which is not possible without field [10, 11]. This helps to get information about the charge density distribution and to compare with theoretical calculations. Especially for intermetallic compounds high external fields are necessary, because with fields which can be produced by electromagnets (max 2 T) the resolution of the spectra is too less, to allow clear conclusions.

In this tutorial the possible great extension of knowledge about magnetic behaviour in solids by application of an external magnetic field is discussed. It is not a review about the field but should give an insight into what is possible on different levels of complexity of magnetic structures. Therefore the presented examples are all from work in which the author was involved. The focus is not only on the results of such investigations but also on how to come to these results, by also discussing possible misinterpretations. In the first part the influence of an external field on the hyperfine interactions and spectral shape is discussed. In the Applications examples from very simple to extremely complex magnetic structures are presented. The last part is devoted to the investigation of dynamic effects by high-field Mössbauer spectroscopy. This tutorial should convince that the investment in a high-field Mössbauer apparatus makes sense and should help to enter the field.

8.2 Hyperfine Field

From the three main hyperfine interactions which are detectable by Mössbauer spectroscopy the most important one for investigating the magnetic ground state properties is the magnetic hyperfine interaction. It is present if the Mössbauer nucleus has a nuclear spin $I > 1$, because in that case it has a dipole moment μ capable to interact with a magnetic field, which might be present at the site of the nucleus. This field can be an internal one, due to the surrounding of the nucleus, or an external one. The magnetic hyperfine field H_{hf}, which the nucleus senses, and which causes the nuclear Zeemann splitting, has two main components

$$H_{hf} = H_{eff} + H_{loc} \tag{8.1}$$

with H_{eff} the effective hyperfine field, and H_{loc} the local hyperfine field. Both can be decomposed into more fields, according to their origin

$$H_{eff} = H_c + H_O + H_d \tag{8.2}$$

with H_c the Fermi contact field, H_O the orbital field, and H_d the dipole field and

$$H_{loc} = H_{ext} + H_{DM} + H_L \tag{8.3}$$

with H_{ext} an external field, H_{DM} the demagnetizing field, and H_L the Lorentz field. The Fermi contact field H_c is due to the Fermi contact interaction of the nuclear moment with the spin density at the nucleus [12]. This density comes partly from an unbalanced spin density of *s*-electrons at the nucleus and partly from conduction electrons [13, 14]. The latter one comes from polarization produced by exchange interactions with the 3d electrons and by admixture with the 3d band. For ionic iron compounds H_c is large and negative. With increasing covalency H_c decreases in ionic compounds [15]. The orbital field H_O arises from unquenched orbital angular momentum of the parent atom for high spin ferric compounds. It is zero, because ferric iron is an S-state ion (^{6}S). In ferrous iron this term can be large and of opposite sign to the Fermi contact field H_c. The dipole field H_d is caused by the arrangement of the atomic moments in the vicinity of the Mössbauer nucleus. For most iron compounds this term is smaller than the Fermi contact and the orbital term. Whereas the Fermi field can be assumed to be independent of the crystal symmetry, because of the polarization of the inner s-shells, the orbital field and the dipole field are strongly symmetry dependent. The demagnetizing field $H_{DM} = -DM$ reduces the hyperfine field. It depends on the demagnetization factor D, which depends on the shape of the sample and the magnetization M. In contrast to measurements on bulk microcrystalline materials, where H_{DM} is negligible small, because of the multidomain structure, it can become dominant in case of monodomain nanoparticles, especially if the hyperfine field is small [16]. The usual Lorentz field $H_L = 4\pi/3$ for cubic symmetry has to be modified by small residue $H_{L'}$ for noncubic symmetry. Because of the quenched orbital moment in high-spin ferric compounds $H_O = 0$, the hyperfine field at low temperatures is always negative and rather large. In ferrous compounds where H_O can be large, the sign of the observed hyperfine field can be positive or negative. Best way to determine the sign is to apply a large external magnetic field (2 T − 5 T) and to observe the field dependence of the measured hyperfine field. In that way Hanna et al. [1] have shown for the first time that in α-Fe the hyperfine field is negative rather than positive, although at that time theory predicted a positive sign. Detailed description of the nature of the hyperfine field can be found in [8, 12, 17, 18].

By the nuclear Zeeman effect the degeneration of the ground and exited states are lifted and the levels split into $2I + 1$ energetically different levels. In case of ^{57}Fe (Fig. 8.1) the exited state ($I = 3/2$) splits into four and the ground state ($I = 1/2$) into two levels. This gives eight different transition energies, from which two are forbidden because of the selection rules for magnetic dipole transitions: $\Delta I = \pm 1$ and $\Delta m = 0$ or ± 1. As a result the Mössbauer line splits into a sextet (Fig. 8.2). The spacing of the outermost lines is the so-called hyperfine field B_{hf}. From the intensity ratio of the six lines information about the orientation of the magnetic field at the nucleus can be obtained, because the intensity of the six lines depend on the angle θ_m between direction of the magnetic field at the nucleus and the γ-ray direction. For the $\pm 3/2 \rightarrow \pm 1/2$ transitions intensity is given by $\frac{3}{4}(1 + \cos^2\theta_m)$, for $\pm\frac{1}{2} \rightarrow \pm\frac{1}{2}$ it is given by $\sin^2\theta_m$, and for $\mp\frac{1}{2} \rightarrow \pm\frac{1}{2}$ it is given by $\frac{1}{4}(1 + \cos^2\theta_m)$. According to these equations the second and fifth line vanish, if the field at the nucleus is parallel to the

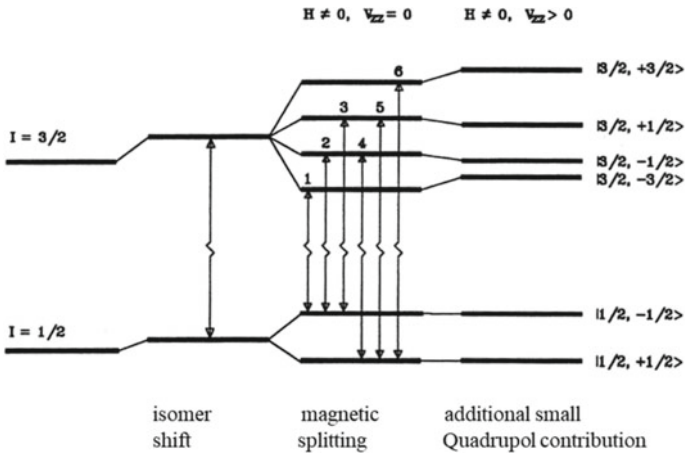

Fig. 8.1 ^{57}Fe level scheme for magnetic dipole interaction (middle) and additional small electric quadrupole interaction (right)

direction of the external field. Then the intensity ratio becomes 3:0:1:1:0:3 (Fig. 8.2b). This situation can be found, if the sample is a single crystal, which is oriented accordingly, or by a high external field, which rotates all hyperfine fields parallel to the applied field direction. In a case where the field is oriented perpendicular to the external field direction the intensity ratio becomes 3:4:1:1:4:3 (Fig. 8.2c). If the sample is polycrystalline, one has to integrate over all possible θ_m values. In this case the obtained intensity ratio is 3:2:1:1:2:3 (Fig. 8.2a). If in addition to the magnetic splitting also electric quadrupole interaction is present, spectra can become very complicate, even with appearance of the forbidden lines. In case the electrostatic interaction is much smaller than the magnetic one, the quadrupole splitting causes a shift in the position of the inner four lines against the outer ones (Fig. 8.1). To get the internal field, the applied field B_a has to be subtracted from the measured hyperfine field B_{hf}. If spectra are not fully polarized the angle θ between B_a and B_{hf} has to be taken into account. The internal field B_{int} is then given by $B_{hf}^2 = B_a^2 + B_{int}^2 - 2B_a B_{int} \cos\theta$. If the applied field is strong enough to polarize the spectra, angle θ becomes zero and the situation is easier. The value of B_{int} is than simply given by the difference $|B_{hf} - B_a|$ (Fig. 8.3). If measured B_{hf} is larger than the applied field B_a, the internal field B_{int} has to be parallel to the applied field. If B_{hf} is smaller than B_a, internal field B_{int} is antiparallel to the applied field.[1]

[1]The internal field B_{int} is sometimes also called induced field B_{ind}, or transferred field B_{trans}, because it is caused by neighbouring ligands. In this tutorial both B_{int} and B_{ind} are used synonymously.

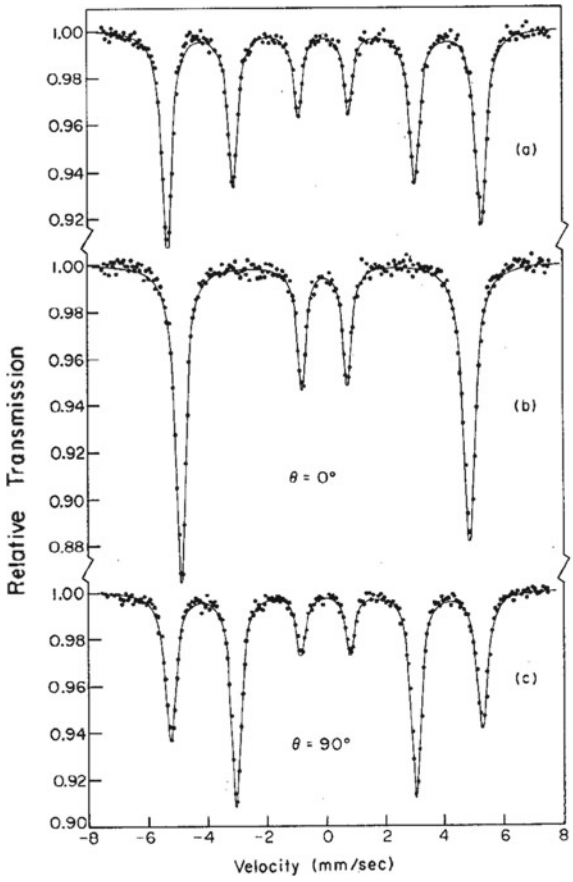

Fig. 8.2 ^{57}Fe Mössbauer spectrum for polycrystalline α-Fe in zero field (**a**), in 5 T parallel to the external field direction (**b**), and in 0.35 T perpendicular to the external field direction (**c**)

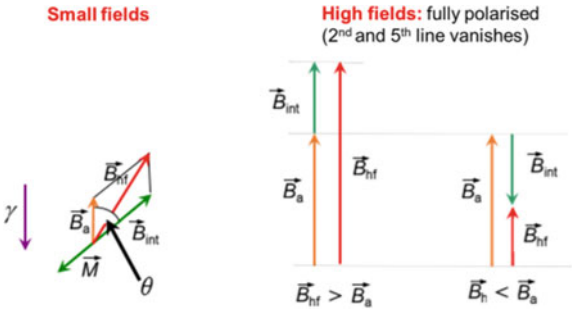

Fig. 8.3 Determination of the internal field B_{int} in case of small (left) B_a and large (right) external fields

8.3 Simple Magnetic Structures

In case of a diamagnet all electronic shells are completely filled. Thus they do not carry a magnetic moment, therefore they do not react on an applied field B_a. In that case the measured hyperfine field B_{hf} at the nucleus is identical to B_a.

In case of an isotropic paramagnet the situation is the following: without external field the spectrum is a single line, or in case of a small electric quadrupole interaction a doublet. Applying an external field induces an internal field B_{ind}. Figure 8.4 shows as a typical example spectra of $Y(Fe_{0.40}Al_{0.60})_2$ at room temperature and different external fields. For all fields the spectra are fully polarized, visible by the vanishing of the 2nd and 5th line of the sextets. The measured hyperfine field $B_{hf} = B_a - B_{ind}$ is practically identical to the applied field B_a. The line shows the calculated influence of B_a. Broadening and small shift of centre of gravity of the lines are due to differences in B_{ind} for different Fe surroundings. The change of measured B_{hf} and calculated small B_{ind} values with applied field B_a is shown in Fig. 8.5.

In ferromagnetic materials magnetization and therefore magnetic hyperfine splitting is present already at zero applied field. Figure 8.6 shows the field dependence of polycrystalline α-Fe 4.2 K for different external fields. Again the line indicates spectra, which would be obtained if only the applied field is present. With increasing

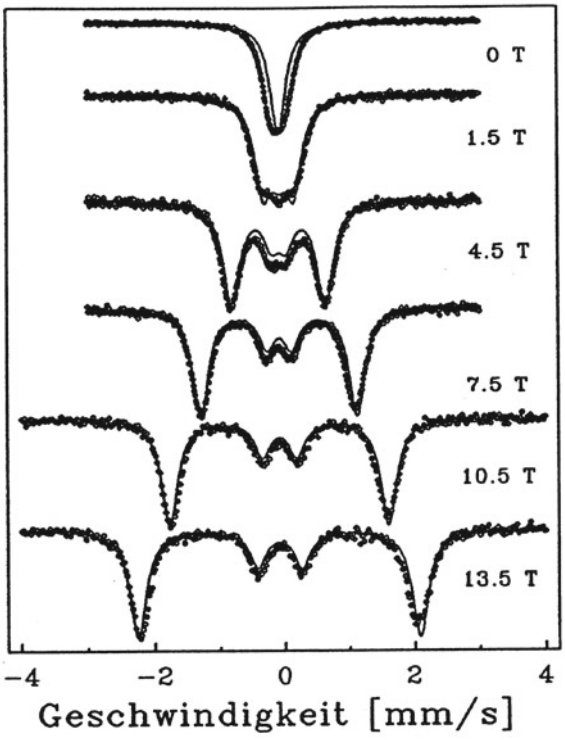

Fig. 8.4 Room temperature spectra at different applied fields for $Y(Fe_{0.4}Al_{0.6})_2$ as an example of a paramagnet. Reprinted from [19]

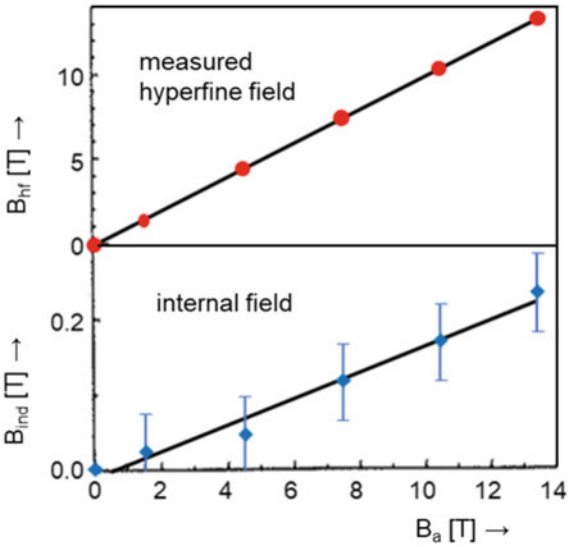

Fig. 8.5 Measured hyperfine field B_{hf} and calculated induced field B_{ind}=|B_a-B_{hf}| versus applied field B_a. Modified from [19]

field domains are rotated in direction of the applied field. Full alignment is reached at approximately 4 T, again visible by the vanishing of the 2nd and 5th line. The measured hyperfine field B_{hf} decreases with increasing B_a, but is always larger than B_a. Therefore the internal hyperfine field B_{int} is antiparallel to the external one. As in an external field the magnetic moments are always rotated into the external field direction, the hyperfine field is antiparallel to the moment in α-Fe. Figure 8.7 shows the change of B_{hf}, B_{int}, and θ with applied field B_a. At zero applied field the angle θ between B_{int} and B_a is 54.735°, which corresponds to random distribution of the fields, and reaches zero at approximately 4 T. The internal field is as expected independent of B_a. The small increase in low external fields is due to the demagnetization field, which is not taken into account in the analysis.

In antiferromagnetic materials the magnetic moments of the two magnetic sublattices compensate on a large scale, but locally magnetic fields are present. These fields lead to magnetic hyperfine split spectra. If there is only one internal field B_{int} several different cases can be found in an external field (Fig. 8.8). If internal fields are parallel to the applied field, two subspectra for the two hyperfine fields $B_{hf} = B_a \pm B_{int}$ are present (Fig. 8.8b). This case can be realized if a single crystal is oriented appropriately in field. In higher external fields it is energetically more favourable if the internal fields are perpendicular to the applied field. In this case again only one subspectrum is present (Fig. 8.8c). This case is visible also for polycrystalline powders if the external field is high enough. Is B_a too low, the spectrum of antiferromagnetic powder samples can become very complex [20].

Many magnetic systems show relaxation behaviour, which leads to time varying hyperfine fields. These relaxation behaviour can have many reasons like energy exchange between spins—so-called spin-spin-relaxation—but also energy exchange

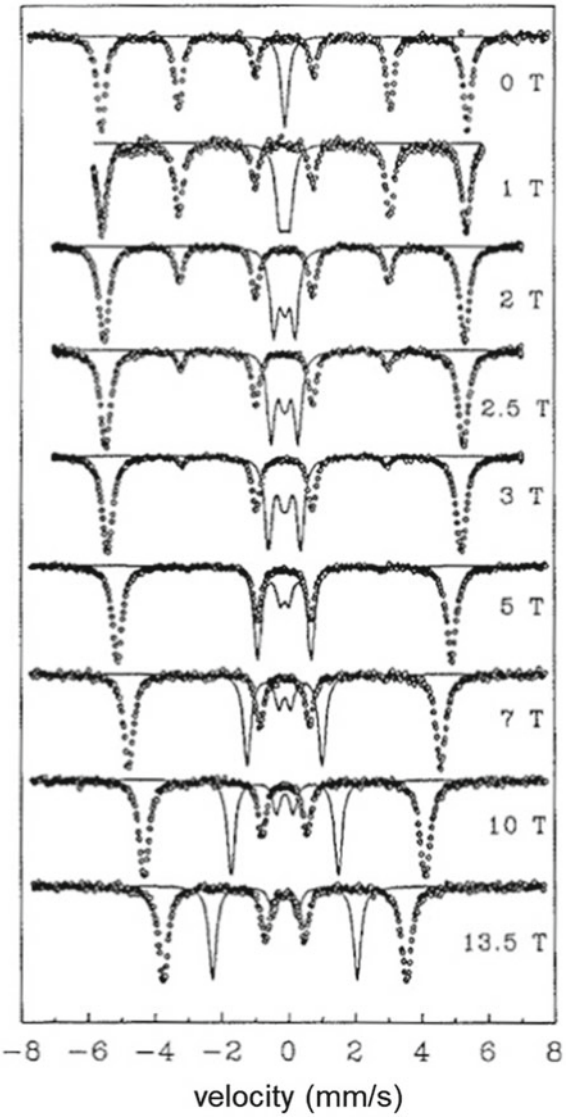

Fig. 8.6 Mössbauer spectra of an α-Fe foil 4.2 K for different applied fields, as example of a ferromagnet. The line is a calculation of the pure field effect. Reprinted from [19]

between the spins and the lattice—so-called spin-lattice-relaxations—to name only a few. These time dependence of hyperfine interactions can strongly influence the shape of the measured spectra, if the corresponding characteristic relaxation time τ_R is in the range of the characteristic time of the experiment. Each measuring method has its own characteristic time window. This is the time during which measurement is performed. In case of a bulk magnetization measurement this is in the range of 1 up to 100 s. Ac-susceptibility measurements are in the range of 1– 10^{-4}s, and

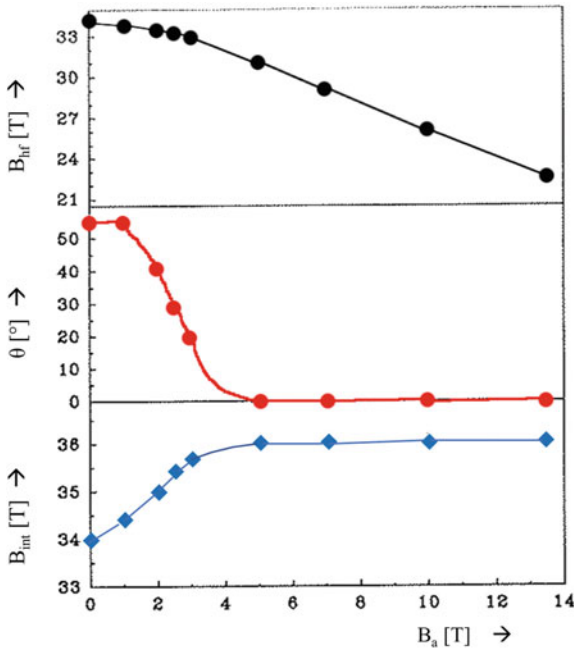

Fig. 8.7 Measured hyperfine field B_{hf}, angle between B_{hf} and B_a, as well as calculated internal field B_{int} over applied field B_a. Adapted from [19]

neutron measurements have a characteristic measuring time of $10^{-8} - 10^{-13}$s. The time window of Mössbauer spectroscopy is determined by the life time of the excited state of the nucleus τ_N. Depending on the Mössbauer isotope τ_N is between 10^{-7} and 10^{-9} s. To measure a magnetic split spectrum, there must be sufficient time for the nucleus to sense the effect of the magnetic field acting on it [21]. This means that at least one Larmor precession must take place before the nucleus decays. Therefore the Larmor precession time τ_L must be smaller than the nucleus life time τ_N. According to the relaxation time τ_R two cases can be distinguished. (i) $\tau_R \gg \tau_L$; this corresponds to slow relaxation. Here the hyperfine fields change so slow during one Larmor precession, that the nucleus senses the full hyperfine interaction. Therefore a static six line spectrum is measured. (ii) $\tau_R \ll \tau_L$; this corresponds to the fast relaxation. Here hyperfine fields change several times their direction during one Larmor precession. Therefore the nucleus senses only an averaged hyperfine interaction. In this time regime the spectra collapse and so-called motional narrowing of the lines take place. In the extreme case the spectrum collapses to a single line. Because the Larmor frequency depends on the magnetic energy, it is different for the different lines of the sextet. The broadening and collapsing of the lines appears therefore first for the inner lines of the sextet, and last for the outermost ones. A detailed discussion of the influence of time windows can be found in [21] and references therein. Figure 8.9 shows the influence of different relaxation times on the shape of the spectrum. The calculation is performed under the assumption that the hyperfine field jumps between +20 T and −20 T. Depending on the type of sample and the relaxation mechanism it

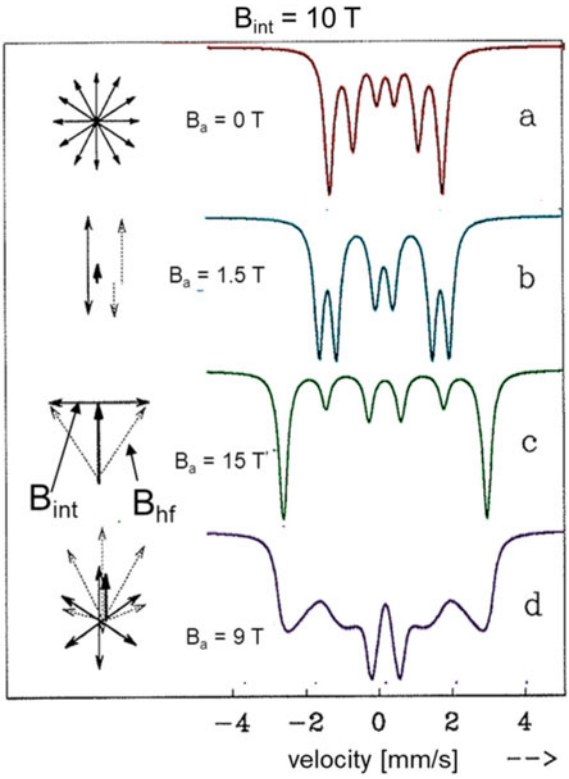

Fig. 8.8 Simulated Mössbauer spectra for different antiferromagnetic moment arrangements. For explanation see text. Reprinted from [19]

is possible with the application of a strong external field to influence the relaxation time τ_R in such a way that it comes in the range of the Larmor precession time τ_L and relaxation spectra are obtained. Information about the characteristic relaxation times and the time dependence of the hyperfine interactions can be gained. Simulation of relaxations spectra are possible by using stochastic methods [22–29], but also by perturbation theory or ab initio calculations [30–34]. In the simplest case the hyperfine field jumps between two states where the fields are antiparallel to each other. Whereas for the left figure equal occupation time of both states is assumed, an occupation of 1–2 of both states is assumed in the case shown in the right figure. No difference is found for the lower relaxation times, but large differences are present in the fast relaxation regime. Figure 8.10 shows results for field flip between +20 T and +8 T on the left, and between +20 T and −8 T on the right side. In both cases the occupation of the states was chosen to be equal. Due to the different field values in the two states the spectra are much more complicate. The influence of different orientations of the hyperfine fields relative to the γ-ray direction is shown in Fig. 8.11. As can be seen, relaxation effects can make spectra rather complicate and are not easy to be correctly analysed. Often dynamical effects in Mössbauer spectra are not

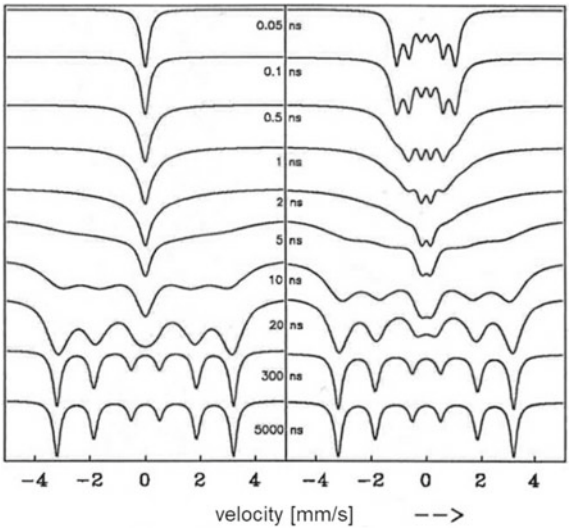

Fig. 8.9 Simulated relaxation spectra for field flip between ±20 T with an occupation probability of 1:1 left and 2:1 right for different relaxation times. Reprinted from [19]

Fig. 8.10 Simulated relaxation spectra for field flip between 20 T and 8 T (left) and 20 T and −8 T (right) for different relaxation times. Reprinted from [19]

so clearly seen [35]. Alternative analyses with static hyperfine field distributions (e.g. [36]) should be taken with care [20].

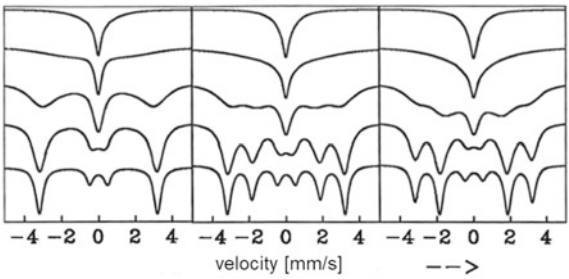

Fig. 8.11 Simulated relaxation spectra for field flip between ±20 T and different angles between the fields, assuming same occupation probabilities. Angle between fields and γ-direction left 0°(left), 54.7°(middle), and 90°(right). Relaxation times from top to bottom: 1, 3, 9, 27, 81 ns. Reprinted from [19]

8.4 Experimental

Different methods are used to apply external fields. Cheapest one, but also in many cases sufficient, is to put a permanent magnet near to the sample. By shaping the magnet as a ring around the sample, a rather homogeneous field at the absorber can be reached. Disadvantage is the rather low value of the reachable field. In general, homogeneity of the field is not critical for the Mössbauer experiment, but it should be uniform in the region where the sample is located. A uniformity of at least 1% over the measuring time, which can last more than one week, should be guaranteed. With electromagnets fields up 2 T are reachable. For higher fields Bitter magnets or superconducting coils are necessary. Commercially available superconducting solenoids for Mössbauer spectrometry have a maximum field around 15 T. For higher fields resistive solenoid magnets made by the Bitter design [37] are used. This magnets are build up by a pile of copper plates with radial slits, separated by isolating plates. The resulting distribution of the current in such coils is inversely proportional to the radius of the plates. Nearly all input energy is transformed into heat. Therefore the plates have holes and channels for transport of cooling water. A typical Bitter magnet has in the 5 cm axial bore a maximum field of 15 T consuming 5 MW power. Fields of up to 37.5 T could be reached with a Bitter magnet at the High Field Magnet Laboratory in Nijmegen, Netherlands. Thus rather high static fields can be reached with Bitter magnets, but they are available only at few places in the world. One main problem with Bitter magnets is their high level of mechanical vibrations resulting from the huge flow of cooling water. Great care has therefore to be taken in order to avoid line broadening or smearing of the spectra. Nowadays high static fields can be produced by superconducting coils made of NbTi (up to 9 T) or Nb_3Sn (up to 21 T). They are expensive and need to be cooled to liquid helium temperature, but are commercially available. Record high static fields of 45 T have been reached in a hybrid Bitter-superconducting magnet at the National High Magnetic Field Laboratory in Tallahassee, Florida. For Mössbauer spectroscopy fields 5 T are often enough

to fully polarize the spectra, which makes interpretation of the measurements easier. In Figs. 8.12 and 8.13 a sketch of the 15 T high field Mössbauer equipment at the Institute of Solid State Physics, TU Wien is shown, which was installed in 1984 by Oxford Instruments. The field is generated by a system of several concentric superconducting coils. The inner ones made of Nb_3Sn and the outer ones by NbTi. The coils are in the liquid helium reservoir of a bath cryostat, which is isolated from the outside by vacuum and a liquid nitrogen shield. The field value is measured by the voltage drop over a shunt resistance placed in series with the coil set and monitored by a Hall sensor. By reducing the temperature of the liquid helium to 2.2 K by the installed lamda fridge, fields up to 15 T can be produced. The maximum field is reduced to 13.6 T if the bath temperature is 4.2 K. To hold fields constant over long time, the magnet can be switched to persistent mode, where a superconducting shortcut over the coil decouples the coil from the power supply and the current is confined in the coil. In this *persistent mode* no field reduction over a period of several days is obtained. Accuracy of field is ± 0.01 T. Field homogeneity of 1% is reached in a cylinder volume 2 mm height 15 mm diameter, where the sample is positioned. To avoid splitting of the source spectrum the ^{57}Co**Rh** source is positioned in a field compensated area, which is produced by a small compensation coil. The driving unit, based on a loudspeaker system, is situated on top of the cryostat. Because of stiffness of the rather long (~ 150 cm) rod which connects the source with the driving unit, only sinusoidal movement is possible. Both sample and source are mounted in the variable temperature insert (VTI), which is inserted in the bore of the magnet (Fig. 8.14). The VTI is separated from the He bath by vacuum. Via two valves liquid He can be inserted into a pot which is in thermal contact with the inner tube where the sample is located, allowing to produce temperatures at the sample between 1.5 K (by pumping above the liquid He) up to room temperature (by heating the He gas). Source and sample are in two rooms, which are separated by a window. With its own heater, the source temperature can be hold constant, independent of the temperature of the sample. Temperature of the absorber is measured by a carbon glass and a $SrTiO_3$ sensor. The first one allows to determine very precisely the temperature, whereas the second one is necessary to correct for the field dependence of the carbon glass. $SrTiO_3$ is a capacitive sensor which is not as sensitive as the carbon glass, but is practically field independent (± 1 mK at 15 T). The combination of both sensors allows to stabilize temperature during a field sweep. As detector a proportional counter is placed on bottom outside of the cryostat. Due to the large distance between source and detector of 50 cm and the seven windows, which the γ-ray has to pass on its way out of the cryostat to the detector, sources with higher activity are necessary. On the other hand the active area of the source is rather small due to the given geometry. Therefore sources with activities of approx. 35 mCi are used. Depending on the type of sample, measuring times of up to two weeks for one spectrum are not seldom, if samples are not enriched with ^{57}Fe. To change samples the whole VTI has to be removed. To avoid air entering the system, a bellow is installed at the top, which can be flushed with helium gas during the removal of the insert. For calibration of the velocity a second source is mounted on the upper side of the driving head with an α-Fe foil, a second proportional counter, and a second

Fig. 8.12 15 T high field Mössbauer equipment at the Institute of Solid State Physics, TU Wien, Austria

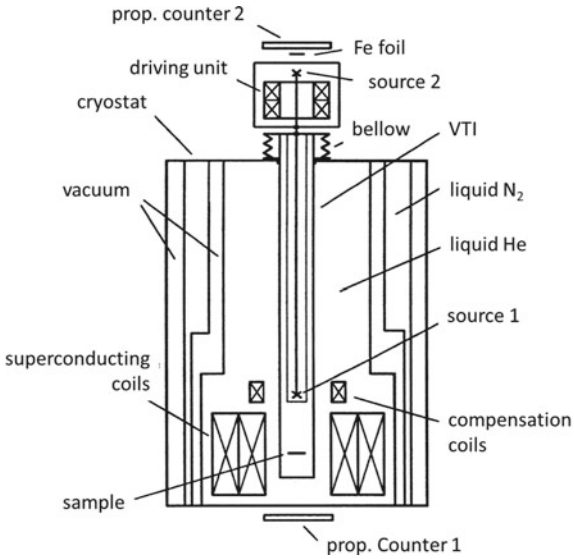

Fig. 8.13 Sketch of high field Mössbauer spectrometer at TU Wien

electronic system. Thus calibration spectra are taken simultaneously to the sample measurements. The stability of temperature and field are permanently checked by software, so that a temperature stability of ± 0.2 K and a field stability ± 0.01 T during the measurements is guaranteed.

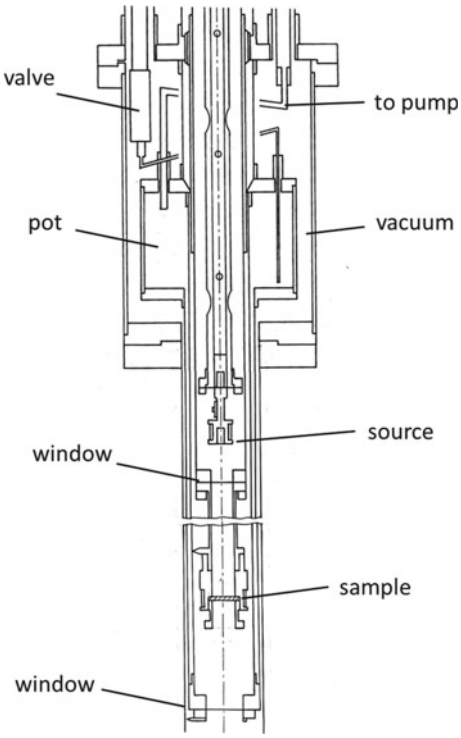

Fig. 8.14 Sketch of the variable temperature insert

8.5 Applications

8.5.1 Ga Substituted Co Ferrite

In spinels, general structure formula AB_2O_4, magnetic ions are usually distributed over the octahedral B and the tetrahedral A sites (Fig. 8.15). In case of a two atom spinel, most prominent representative is magnetite, Fe_3O_4. For spinels, where more than one atom can occupy the A and B sites, the distribution of magnetic atoms over these sites is one of the important points for understanding the magnetic behaviour. If all A-atoms are occupying the B-sites and 50% of the B-atoms are on the A-sites than one has a so-called inverse spinel. In case of not full occupation of A-atoms on the B-sites one speaks of partial inverse spinel. For example, in case of Ga substituted Co ferrite no clear picture concerning the site distribution of the three elements Co, Ga, and Fe was obtained from different measurements. X-ray diffraction investigations indicated that Co mainly occupies only B-sites, thus suggesting an inverse spinel [38]. In contrast from neutron diffraction measurements on pure $CoGa_2O_4$ only 60% of the Ga atoms were found on the cobalt A-sites, thus pointing to partial inverse spinel [39]. ^{57}Fe Mössbauer spectroscopy on $CoGa_{2-x}Fe_xO_4$ at room temperature show two clearly separated components with different intensities, pointing to a partial inverse

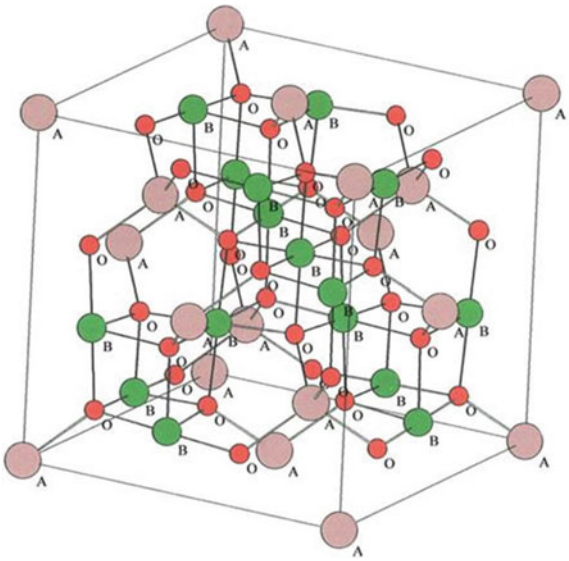

Fig. 8.15 Spinel structure AB_2O_4, with A the tetrahedral and B the octahedral sites

spinel. It was concluded that samples with higher Fe content show ferromagnetism, whereas a spin glass behaviour was proposed for the low Fe regime [40]. A final clarification was possible by ^{57}Fe Mössbauer measurements in external fields. In the following results of measurements on $CoGa_{2-x}Fe_xO_4$ samples with $x = 0.2, 0.3, 0.8$, and 1.0 in temperature 5 K to room temperature and at external fields 0, 4, 9, 13.5 T are discussed. In contrast to the zero field spectra, in-field spectra are much more complex and cannot be interpreted anymore by superposition of only two subspectra (Fig. 8.16).

Good results are obtained for the Fe-rich samples with $\Gamma/2 = 0.18$ mm/s, whereas $\Gamma/2 = 0.20$ and 0.24 mm/s are found for samples $x = 0.3$ and 0.2 on the Fe poor side. $\Gamma/2$ further increases on the Fe poor side with increasing applied field. This increase with B_a is an indication of increasing influence of relaxation effects. Especially at higher temperature typical relaxation spectra are measured (e.g. 25 K in (Fig. 8.16)). This corresponds well with findings of dc magnetic measurements, where magnetization curves typical for spin glasses are obtained. Transition temperatures of 26 and 32 K for $x = 0.2$ and 0.5 were obtained. On the Fe rich side relaxation spectra appear only above approximately 200 K (Fig. 8.16).

For analysis of the spectra below the relaxation regime (Fig. 8.17) a complex model, based on possible nearest neighbour surroundings is necessary to explain the measured Mössbauer spectra. Assuming that all three elements (Co, Ga, Fe) can occupy both A and B sites, the general formula of the compound is given by $(Co_\lambda Ga_{1-\lambda-y} Fe_y)_A (Co_{1-\lambda} Ga_{1+\lambda-z} Fe_z)_B O_4$ with $y + z = x$, according to a partial spinel. The final fit was performed with a superposition of several subspectra with intensity ratios determined by means of binomial distributions according to the different possible nearest neighbor (*nn*) surroundings. Taking into account only

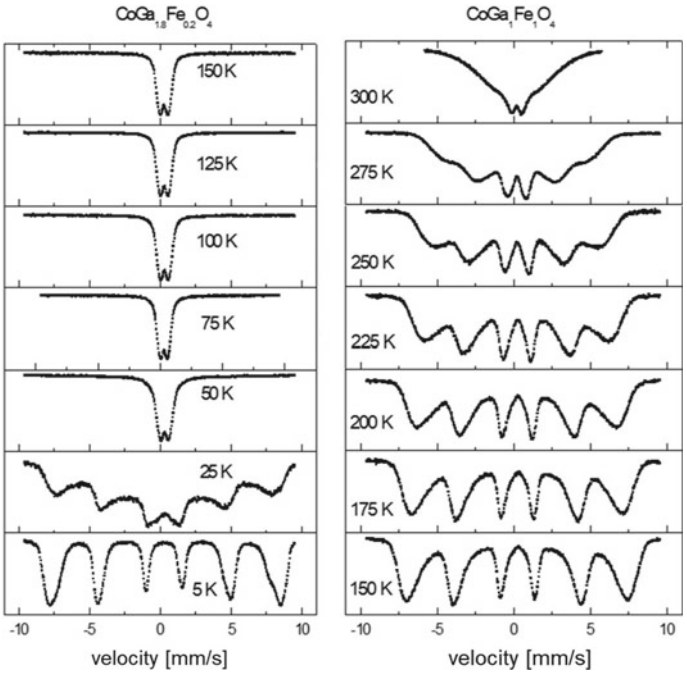

Fig. 8.16 ^{57}Fe Mössbauer spectra for $x = 0.2$ (left) and $x = 1.0$ (right) for selected temperatures

spectra with relative intensities larger than 1%, for A-sites, which have 12 *nn* (nearest neighbour) B atoms, 7–8 subspectra and for the B-sites, which have 6 *nn* B-atoms, between 5 and 6 subspectra were used in the fits. Electric quadrupole splitting, isomer shift and angle θ between external and hyperfine field were equal for the subspectra which correspond to A and B-sites respectively. $\Gamma/2$ was kept constant for all subspectra. Only B_{hf} varied between the different subspectra for the two sites. Further it was assumed, that hyperfine field increases with increasing *nn* Fe number. Under these assumptions the change of magnetic hyperfine field with applied field B_a gives detailed information about magnetic behaviour. Whereas B_{hf} increases linearly with B_a for the subspectra according to site A, B_{hf} decreases linearly with B_a for all subspectra which correspond to site B (Fig. 8.18 and lines in Fig. 8.17). With the obtained absolute value of the measured hyperfine field B_{hf} and the obtained angle θ between hyperfine field and applied field B_a the internal field B_{int} can be determined. In this way in Table 8.1 obtained B_{int} values are given together with B_{hf}, θ and B_a for both sites A and B for two samples on the Fe rich ($x = 1.0$ and 0.8) as well as on the Fe poor ($x = 0.3$ and 0.2) side. As expected, calculated B_{int} values are independent of applied field, but increase slightly with increasing Fe content x. Due to the demagnetizing field the hyperfine fields are 1 T lower at the A-site and higher at the B-site compared to the zero field values.

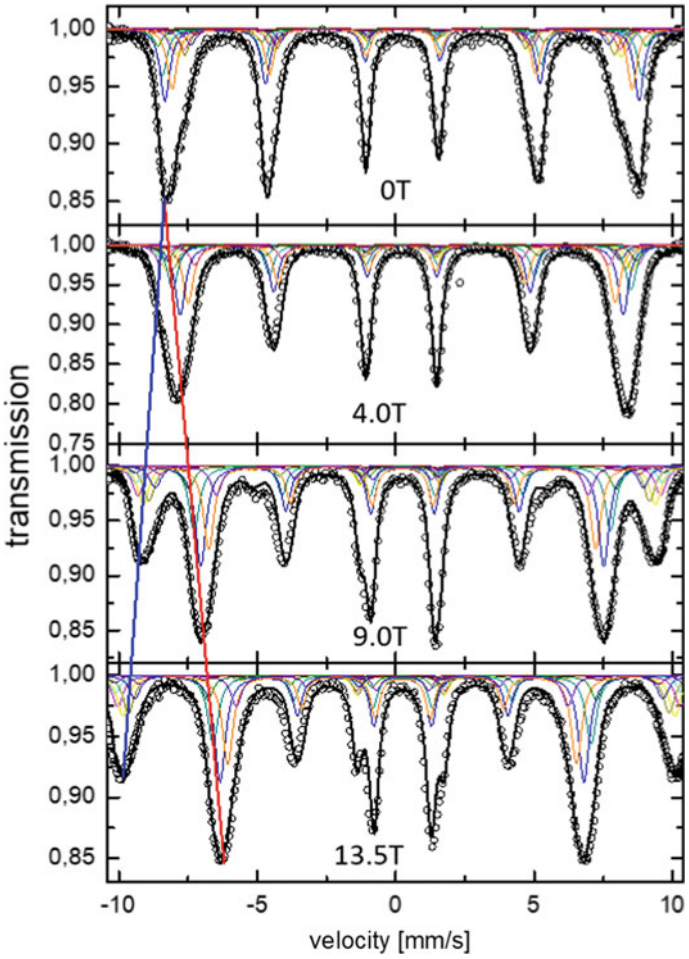

Fig. 8.17 ^{57}Fe Mössbauer spectra for $CoGa_{1.2}Fe_{0.8}O_4$ for selected fields at 4.2 K

From the obtained θ values it is seen that B_{int} is parallel to B_a, with deviations of up to 18° for A-sites. This deviations decrease with increasing Fe content x. For the B-sites B_{int} points in the direction antiparallel to B_a with deviations up to 57°. This indicates that Fe moment on A-sites are antiparallel to the Fe-moment on the B-sites. The fact that B_{int} increases with x and θ decreases with x points to an increase in coupling strength with increasing Fe content. Assuming that there is a direct proportionality between internal hyperfine field B_{int} and the magnetic moment, the fact that B_{int} is larger on B-sites than on A-sites indicates that the resultant B_{int} is antiparallel to B_a and therefore the overall moment, which is antiparallel to the internal field, is parallel to the applied field. This is in good agreement with the fact that in dc magnetic measurements a ferromagnetic like behaviour is obtained [40].

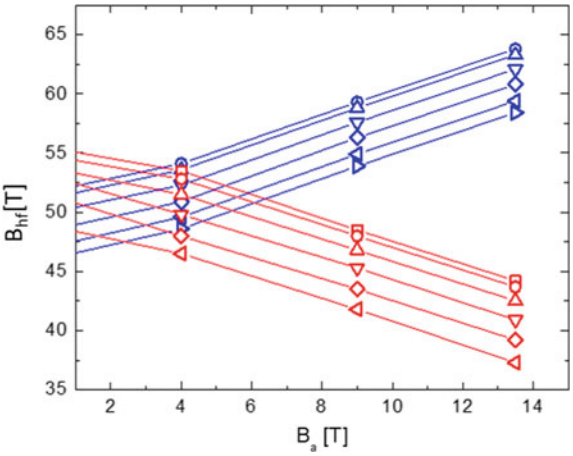

Fig. 8.18 Measured hyperfine field B_{hf} over applied field B_a for $CoGa_{1.2}Fe_{0.8}O_4$

Table 8.1 Mean values of measured hyperfine field B_{hf}, angle Θ between B_{hf} and applied field B_a and calculated internal field B_{int} for both A- and B-sites for different B_a and Fe concentration x [41]. Reprinted by permission from Springer: Hyperfine Interactions, High field Mössbauer investigations of $CoGa_{2-x}Fe_xO_4$ spinels, M. Reissner, W. Steiner, Z. Seidov, G. Sultanov, copyright (2002)

x		1,0			0,8			0,3			0,2		
	B_a	B_{hf}	θ	B_{int}	B_{hf}	θ	B_{int}	B_{hf}	θ	B_{int}	B_{hf}	θ	B_{int}
	[T]	[T]	[°]	[T]	[T]	[°]	[T]	[T]	[°]	[T]	[T]	[°]	[T]
A	0	50.1			49.0			46.8			46.2		
	4	53.2	12	49.1	51.7	18	47.9	49.2	18	45.4	49.2	18	48.0
	9	58.4	12	49.2	56.9	18	48.4	53.7	18	45.2	54.1	18	45.6
	13.5	62.9	5	49.6	61.4	18	48.7	58.4	18	45.8			
B	0	53.3			52.0			51.6			50.5		
	4	49.8	210	53.5	49.5	230	52.2	49.0	232	51.6	48.1	237	50.4
	9	45.0	205	53.3	44.8	218	52.2	44.7	230	51.0	43.0	230	49.3
	13.5	40.4	202	53.2	40.4	214	52.1	40.2	225	50.7			

With increasing x the number of iron atoms on A-sites decrease, whereas it increases on B-sites. The ratio for iron on A-sites (y) and Fe on B-sites (z) increases with x. It is 0.25, 0.33, 0.54, and 0.64 for x = 0.2, 0.3, 0.8, and 1.0, respectively. The same tendency was found by the X-ray investigations [38]. The application of external fields allowed to show that the different field dependence of the two components found in the spectra proves that both A- and B-sites are occupied by iron atoms. The different intensities of these two components prove that the samples are partial inverse spinels. A antiferromagnetic coupling is found between Fe on A- and B-sites. The values of the internal fields are around 10% higher for the iron atoms at the B-sites and are only mildly dependent on x.

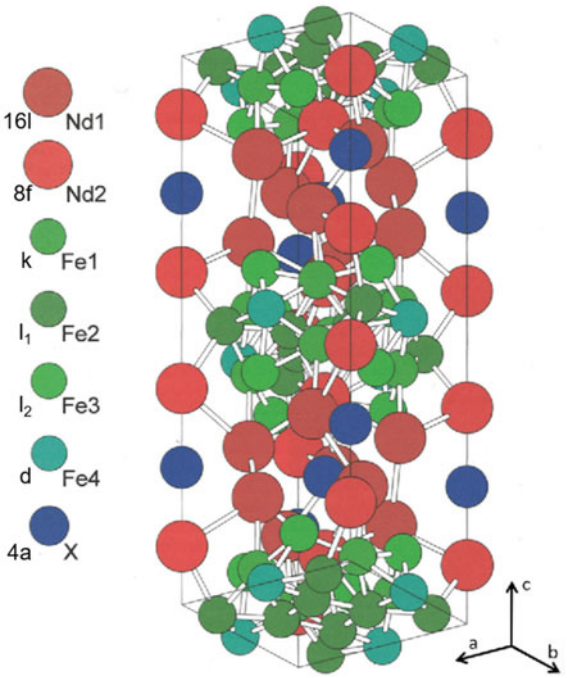

Fig. 8.19 Structure of $RE_6Fe_{13}X$ compounds

8.5.2 $RE_6Fe_{13}X$ compounds

$RE_6Fe_{13}X$ compounds where RE are light rare earth atoms and X are main group atoms from the 3rd to the 5th row of the periodic table are intensively investigated. These compounds are of interest, because they are by-products in the preparation of $Nd_2Fe_{14}B$ permanent magnets, where small additions of X metals improve wettability and corrosion resistance [42–49]. Acting as pinning centers for domain wall movement, they also have a large influence on the coercivity of the Nd-Fe-B permanent magnets [50, 51]. The crystallographic structure of $RE_6Fe_{13}X$ compounds is $Nd_2Fe_{14}B$, space group I4/mcm [52]. There are four different iron sites, namely 16k, $16l_1$, $16l_2$, and 4d (Fig. 8.19). The RE-atoms occupy the two crystallographic sites 16l and 8f. A strong influence of the RE atoms on the magnetic behaviour was found [54, 55]. From different measurements (X-ray, neutron, magnetic and Mössbauer) a ferrimagnetic or antiferromagnetic arrangement of the moments was concluded. Because of rather low magnetization values of $\mu_{sat} \leq 8\mu_B$ Weitzer et al. [52, 56] suggested a ferrimagnetic coupling within the Fe sublattice, although a canting of the RE moments could not be ruled out. On the other hand ^{57}Fe Mössbauer investigations [54] have shown, that hyperfine fields obtained from measurements take at 4 K are large and very similar for the different compounds. According to the existence of four different Fe-sites four sub-spectra with intensity ratio of 4:4:4:1 according to the k, l_1, l_2, and the d sites are expected. This holds for many of the compounds e.g.

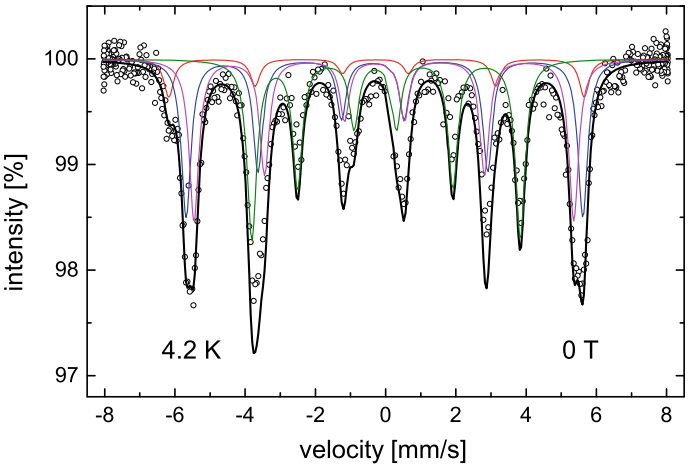

Fig. 8.20 Zero-field ^{57}Fe Mössbauer spectra of $Nd_6Fe_{13}Sn$ at 4.2 K [53]. Reprinted from J. Mag. Mag. Matter, 226–230, R. Ruzitschka, M. Reissner, W. Steiner, P. Rogl, Magnetic and high field Mössbauer investigations of $RE_6Fe_{13}X$ compounds, 1443–5. Copyright (2001), with permission from Elsevier

$Nd_6Fe_{13}X$ with X = In, Sn, Tl, Pb [54] (Fig. 8.20). Such interpretation holds, if the contribution of anisotropic dipole fields to the hyperfine fields are so small that they can be neglected. If they are not negligible small, the possibility to fit the spectra with the intensity ratio given by the occupation ratio of the lattice sites indicates, that the easy axis of the magnetization is the *c*-axis. In that case a uniform distribution of dipole fields is obtained, which only changes the magnitude of the hyperfine fields. In case of a deviation of the easy axis from the *c*-direction, due to the various dipole field contributions, the degeneracy of magnetically equivalent lattice sites may be lifted leading to several subspectra, the number of which are determined by the local symmetry [57].

In that case more subspectra are needed for one lattice site. For the given structure no change is expected for the $16l_1$, $16l_2$, and 4d sites, but a splitting in two components is expected for the 16k sites [54]. In case of the easy axis within the basal plane along one of the edges an intensity ratio of 1:1 for these sites is expected (e.g. $Pr_6Fe_{13}Pd$ Fig. 8.21). Indeed, for many compounds ($Nd_6Fe_{13}X$, with X = Cu, Ag, Au and for $Pr_6Fe_{13}X$, with X = Cu, Ag, Au, In, Sn, Tl, Pb) in contrast to four subspectra five subspectra with intensity ratio 2:2:4:4:1 are necessary to fit the measured spectra (Figs. 8.20 and 8.21). Interestingly the values of the obtained hyperfine fields for the different sites are rather independent of the RE and X elements. On the other hand there is a large spread in the value of the hyperfine fields for the different sites, varying by more than 30% [52]. With the obtained hyperfine fields and assuming a direct relation between hyperfine field and magnetic moment, various ferrimagnetic arrangements of moments on the different lattice sites were proposed to explain the rather small Fe-moments obtained in lower fields [52]. Yan et al. [58] and Wang

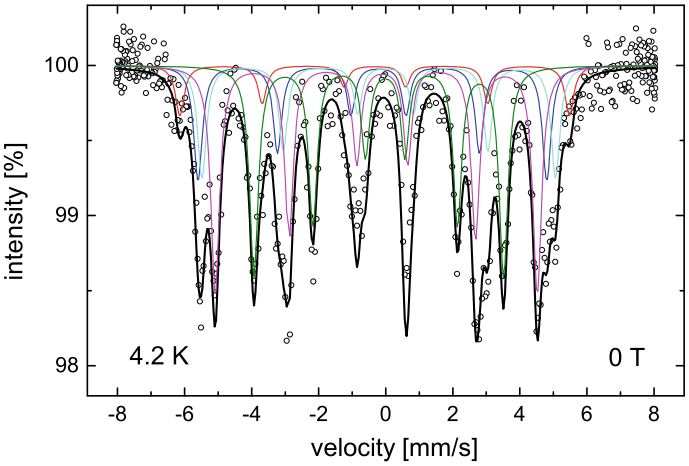

Fig. 8.21 Zero-field ^{57}Fe Mössbauer spectra of $Pr_6Fe_{13}Pd$ at 4.2 K [53]. Reprinted from J. Mag. Mag. Matter, 226–230, R. Ruzitschka, M. Reissner, W. Steiner, P. Rogl, Magnetic and high field Mössbauer investigations of $RE_6Fe_{13}X$ compounds, 1443–5. Copyright (2001), with permission from Elsevier

et al. [59] proposed from X-ray and neutron measurements that the RE moments and the Fe 4d moments are parallel and antiparallel to the other Fe atoms with an easy axis in c-direction for $Nd_6Fe_{13}Si$ and $Pr_6Fe_{13}Si$. In contrast, Schobinger-Papamantellos et al. [60, 61] proposed also from neutron investigations for $Pr_6Fe_{13}Si$ collinear antiferromagnetic ordering of the four Fe and of the two RE sublattices, with the easy axis perpendicular to the c-direction. For $Pr_6Fe_{13}Sn$ and $Nd_6Fe_{13}Sn$ best interpretation of the neutron data were obtained by assuming that all moments in the blocks defined by all atoms inbetween the X-atom layers are ferromagnetically ordered [62]. The blocks itself are antiparallel to each other. The difference between the two samples is, that in case of Pr the easy axis is perpendicular to the c-direction and parallel in case of the Nd compound. The picture becomes even more complex with the result of dc magnetic measurements in higher applied fields, where at low temperatures jumps in the magnetization curves are found. Figure 8.22 shows for example magnetization curves for $Pr_6Fe_{13}Pd$, with a strong jump around 7 T at 2.5 K and obviously saturation at 15 T. With the free ion value of 3.58 μ_B for Pr and the obtained value of 37.5 μ_B/fu at 14.5 T and 2.5 K a Fe-moment of only 1.23 μ_B is obtained. This is much lower than values of compounds with similar RE/Fe ratio like $REFe_2$ with moments of about 1.77 μ_B/Fe [63]. In contrast, for $Nd_6Fe_{13}Sn$ no saturation is found at lowest temperatures and highest fields (4.2 K, 15 T). Here at 8 T a jump in magnetization is present, followed by a second one at 13 T for $T <$ 80 K (Fig. 8.23). The field of the jumps is nearly temperature independent. Such jumps are typical for metamagnetic materials where an antiferromagnetic moment arrangement at low temperatures change with increasing field to a ferromagnetic one by reversal of the moments of one of the two sublattices into the direction of

applied field. In case of the $RE_6Fe_{13}X$ compounds the jumps are too small to be explained by reversal of one of the ferromagnetically coupled sublattices present in the above mentioned proposed antiferromagnetic ordered moment arrangements, indicating that the till then proposed models are too simple. This is confirmed by ^{57}Fe Mössbauer high field measurements. Figures 8.24 and 8.25 show two typical spectra measured 4.2 K at 13.5 T. Comparison with the measurements on the same samples in zero field (Figs. 8.20 and 8.21) show quite different shape. The sharp structure of the spectra in zero field is washed out by very flat side wings in the in-field spectra. Therefore the in-field spectra can by no means be fitted by only 4 ($Nd_6Fe_{13}Sn$) or 5 ($Pr_6Fe_{13}Pd$) subspectra according to the different Fe-sites. A further subdivision of the 4 (5) subspectra was necessary. By restricting the overall number of subspectra to nine, 4, 2, 2, and 1 spectra are used for the k, l_1, l_2, and d site, respectively, keeping the intensity ratio of 4:4:4:1 for the 4 sites. The fit gives values for the magnitude of the hyperfine field and the angle θ between measured hyperfine field at the Fe nucleus and the γ-ray direction. From the difference of hyperfine field and applied field B_a, by taking into account θ, the internal field B_{int} could be determined. The obtained mean values for each crystallographic iron site are in good agreement with the values obtained from the zero-field measurements in case of $Nd_6Fe_{13}Sn$. The projection of B_{int} on the B_a direction gives 55% of the value of B_{int}. This 55% are also obtained by comparing the magnetic moment at 13.5 T and 4.2 K to the moment calculated assuming full alignment of RE^{3+} moments and Fe moments of 1.77 μ_B. For the $Pr_6Fe_{13}Pd$ compound at 13.5 T, B_{int} values which are higher than those at zero field are necessary to get agreement with the degree of saturation found in magnetization. On the other hand, taking both the RE and Fe moment of the neutron refinement [62] leads to a saturation moment which is much higher than the one observed. This together with the found deviations of hyperfine field from complete alignment with B_a indicates a further jump of magnetization at even higher applied fields. The high number of subspectra for the different Fe-sites needed to get reasonable in-field fits points to a magnetic structure which is not simply antiferromagnetic but indicates strong tilting of the spins around the antiferromagnetic alignment of the individual iron layers.

8.5.2.1 Skutterudites

The mineral skutterudite $CoAs_3$ has given its name to a large class of substances. Its structure was first solved by Oftedal in 1928 [64]. Binary skutterudites MPn_3 are formed by many atoms, with M = Co, Rh, Ir and Pn stands for pnictides (P, As, and Sb). The structure consists of a three-dimensional array of slightly distorted octahedra formed by the pnictide atoms, with the M atom in the center. The octahedra are tilted in such a way, that a rectangular arrangement of Pn atoms form, which connect the adjacent octahedra. Due to this tilting large cage-like voids are created in the structure, which can be filled by electropositive atoms A forming the large class of ternary skutterudites $A_xM_4Pn_{12}$ (Fig. 8.26).

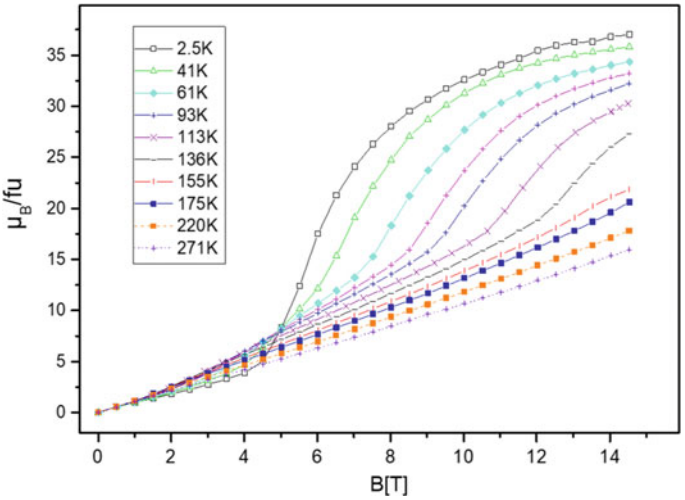

Fig. 8.22 Field dependence of magnetic moment of $Pr_6Fe_{13}Pd$ for different temperatures [55]. Reprinted from J. Mag. Mag. Matter, 242, R. Ruzitschka, M. Reissner, W. Steiner, P. Rogl, Investigation of magnetic order in RE6Fe13X (RE = Nd, Pr; X = Pd, Sn, Si), 806–8. Copyright (2002), with permission from Elsevier

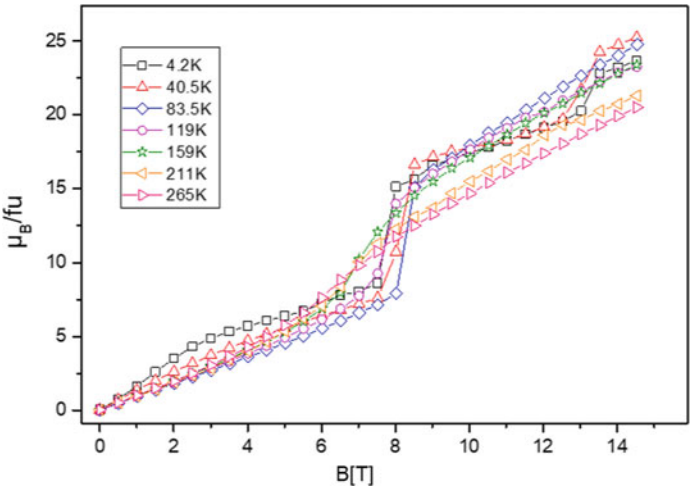

Fig. 8.23 Field dependence of magnetic moment of $Nd_6Fe_{13}Sn$ for different temperatures [55]. Reprinted from J. Mag. Mag. Matter, 242, R. Ruzitschka, M. Reissner, W. Steiner, P. Rogl, Investigation of magnetic order in RE6Fe13X (RE = Nd, Pr; X = Pd, Sn, Si), 806–8. Copyright (2002), with permission from Elsevier

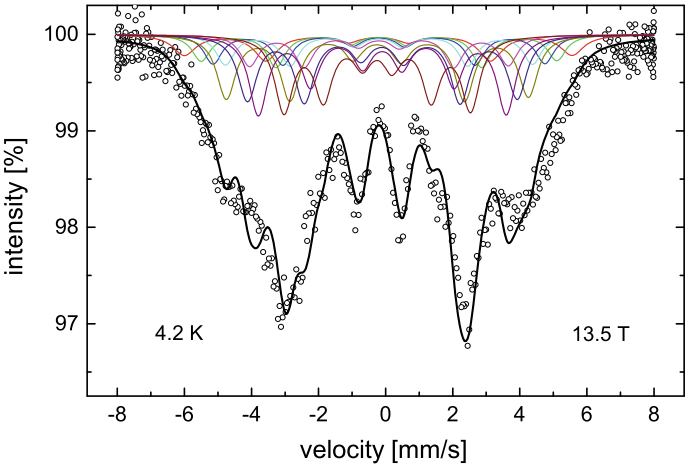

Fig. 8.24 ^{57}Fe Mössbauer spectrum of $Nd_6Fe_{13}Sn$ taken at 13.5 T and 4.2 K [53]. Reprinted from J. Mag. Mag. Matter, 242, R. Ruzitschka, M. Reissner, W. Steiner, P. Rogl, Magnetic and high field Mössbauer investigations of $RE_6Fe_{13}X$ compounds, 1443–5. Copyright (2001), with permission from Elsevier

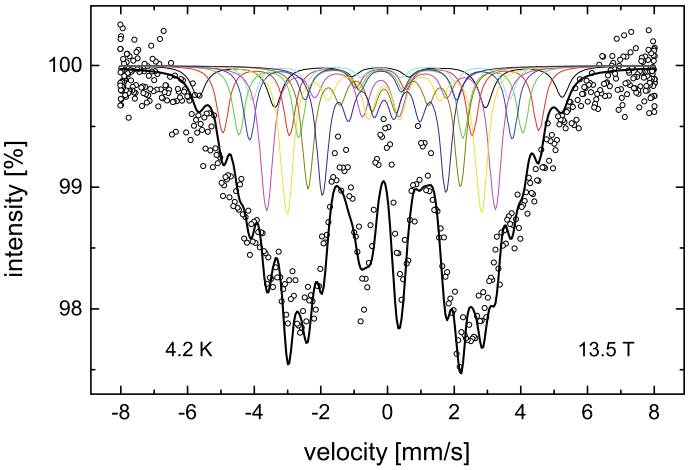

Fig. 8.25 ^{57}Fe Mössbauer spectrum of $Pr_6Fe_{13}Pd$ taken at 13.5 T and 4.2 K [53]. Reprinted from J. Mag. Mag. Matter, 242, R. Ruzitschka, M. Reissner, W. Steiner, P. Rogl, Magnetic and high field Mössbauer investigations of $RE_6Fe_{13}X$ compounds, 1443–5. Copyright (2001), with permission from Elsevier

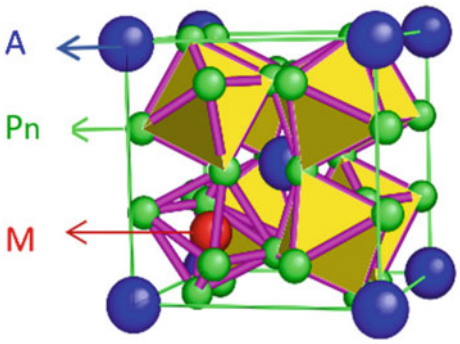

Fig. 8.26 Crystal structure of filled skutterudites

Table 8.2 Intensities of the two subspectra necessary to fit the Mössbauer spectra of $RE_xFe_4Sb_{12}$ compounds and effective magnetic moments from susceptibility measurements

RE-atom	x	Int1/%	Int2/%	μ_{eff}/μ_B
La	0.80	78	22	3.0
Pr	0.73	64	36	4.2
Nd	0.72	69	31	4.5
Eu	0.88	84	16	8.4
Yb	1.00	100	0	4.5

These ternary skutterudites are one example of so-called cage compounds. The first ternary skutterudite $LaFe_4P_{12}$ was synthesized by Jeitschko et al. in 1977 [65]. Since then a large amount of such compounds were found. As filler atoms (A) trivalent light RE (La, Ce, Pr, Nd, Sm, Eu) elements and Yb, as well as Th and U were successfully build into the structure. But also divalent ions as earth alkali (Ca, Sr, Ba) and also monovalent alkali ions (Na, K) and also Tl could be incorporated into the structure. Heavy RE skutterudites (Ho, Er, Tm) could be synthezised under high pressure. In contrast to binary skutterudites, in the ternary compounds also Fe, Os, and Ru are possible on the M site. Skutterudites are of special interest, because of their potential for thermoelectric applications [66–70]. Thermoelectric materials can convert heat in electricity. They are used as power generators in satellites, to cool computer chips and to convert heat of exhaust fumes of trucks.

To be a good thermoelectric material the figure of merit $ZT = S^2(\lambda/\sigma)$ with S the Seebeck coefficient, λ the thermal conductivity and σ the electrical conductivity should be at least 1. Such high value is possible, if good electrical conductivity is, against Wiedemann-Franz law, accompanied by low thermal conductivity, which is possible, if there are low lying Einstein modes in the phonon spectrum, which can be realized by the filler ions which are only weakly bonded in the oversized cages and therefore tend to rattle, thus hindering phonon propagation. In that sense filled skutterudites are archetypes of so-called phonon glass electron crystals, a concept introduced by Slack in 1995 [71].

Beside the high importance for applications, these materials are of interest because of the large variety of possible ground states. Depending on the RE atom features like superconductivity in $LaRu_4As_{12}$ (T_c = 10.3 K) [72], $LaOs_4As_{12}$ (T_c = 3.2 K) [72], $PrRu_4Sb_{12}$ (T_c = 1 K) [73], $PrRu_4P_{12}$ (T_c = 2.4 K) [74], where for the last compound a metal insulator transition is present at 60 K [75], long range magnetic order in $EuFe_4Sb_{12}$ (T_{mag} = 84 K) [76, 77], heavy fermion behaviour in $YbFe_4Sb_{12}$ [78], non-Fermi liquid behaviour in $CeRu_4Sb_{12}$ [79], mixed valence behaviour in $RE(Co,Fe)_4Sb_{12}$ with RE = Yb and Eu [80, 81], are found. In case of the Fe containing skutterudites also a large variety of magnetic ground states is reported. E.g. $REFe_4P_{12}$ compounds with RE = Nd, Eu, Ho are ferromagnetic with ordering temperatures 1.9 K, 80 K, and 5 K, respectively [76]. Also $SmFe_4Sb_{12}$ is ferromagnetic below 45 K. $NaFe_4Sb_{12}$, and KFe_4Sb_{12} skutterudites are itinerant ferromagnets with ordering temperatures 85 K for both [82]. $TlFe_4Sb_{12}$ was found to be a weak itinerant ferromagnet [83]. $PrFe_4Sb_{12}$ is antiferromagnetic with Neél temperature of 4.6 K [84]. For $PrFe_4P_{12}$ antiferroquadrupolar interactions play an important role below 6.2 K [85–87]. AFe_4Sb_{12} compounds with A = Ca, Sr, Ba, Tm, and Yb are paramagnetic respectively nearly ferromagnetic [83]. As mentioned above $LaFe_4P_{12}$ is superconducting below 4 K [88], whereas $LaFe_4Sb_{12}$ is an enhanced paramagnet [76, 82]. One important question is, how the Fe-atoms contribute to the magnetic behaviour. In spite of large amount of theoretical and experimental investigations a precise knowledge about Fe-moments and their interplay with the filler atoms are still missing [70]. E.g. the $LaFe_4P_{12}$ compound is as mentioned above superconducting, indicating that Fe has no moment, although from susceptibility measurements a room temperature effective moment of 1.46 μ_B/fu is obtained. Because La^{3+} has no magnetic moment, the measured one has to be attributed to the (Fe_4Sb_{12}) building blocks. Band structure calculations on $La(Co,Fe)_4P_{12}$ indicate hybridization of the La sites with Sb and Fe states resulting in an enhanced effective mass for the two highest occupied bands [89]. Furthermore a double peak structure of the 3d-DOS in the proximity of the Fermi energy was obtained, from which the presence of a non-zero moment on the Fe site was concluded [90]. Newer studies pointed out that spin fluctuations are important and that this compound seems to be near to a ferromagnetic quantum critical point [91]. The question about the contribution of Fe to the magnetization is further puzzling, if the Sb compounds are considered which show effective moments of several μ_B depending on the type of filler atom (Table 8.2). It should be mentioned that in contrast to the Fe skutterudites based on P, in the Sb based Fe skutterudites the RE sublattice is not always fully occupied. In case of the $Pr_{0.73}Fe_4Sb_{12}$ compound an effective moment of 4.19 μ_B/fu is found from magnetic measurements. Figure 8.27 shows magnetization curves at different temperatures. The compound orders around 5 K [84]. Above 52 K the bending of the magnetization curves disappears. The susceptibility determined from the slope of the $M(B_a)$ curves measured at various temperatures is shown on right side of Fig. 8.27. From this an effective moment of 4.19 μ_B and a paramagnetic Curie temperature θ_p = 0.5 K is obtained in good agreement with findings of [76]. Assuming that the Pr moment is the one of the 3+ ion, the moment of the (Fe_4Sb_{12}) block can be calculated. With the assumption that the contributions are simply additive according to

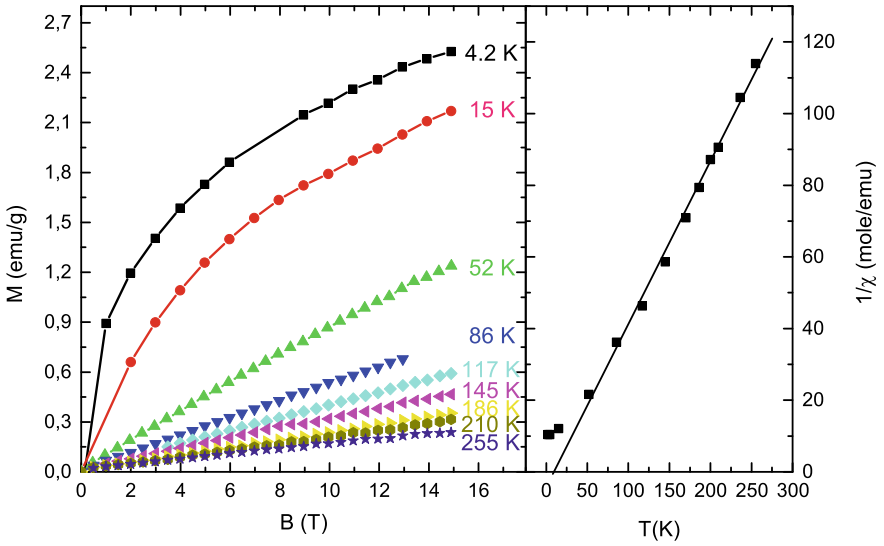

Fig. 8.27 Left: field dependence of magnetization at different temperatures for $Pr_{0.73}Fe_4Sb_{12}$. Right: temperature dependence reciprocal susceptibility [92]. Reprinted from J. Mag. Mag. Matter, 272–276, M. Reissner, E. Bauer, W. Steiner, P. Rogl, High field Mössbauer and magnetic investigations of $Pr_{0.73}Fe_4Sb_{12}$, 813. Copyright (2004), with permission from Elsevier

$$\mu_{eff}^{meas} = \sqrt{x \cdot (\mu_{eff}^{Pr})^2 + (\mu_{eff}^{Fe_4Sb_{12}})^2}$$

with x the filling factor of the RE sublattice, a rather high effective moment for the (Fe_4Sb_{12}) building block of 2.7 μ_B is obtained. Similar high effective moments of 3.0 μ_B and 3.7 μ_B are obtained for $LaFe_4Sb_{12}$ and $CaFe_4Sb_{12}$ [76], which have to be primarily attributed to the magnetic behaviour of Fe. The result that Fe carries a moment in the $Pr_xFe_4Sb_{12}$ skutterudite is in full contrast to $PrFe_4P_{12}$, where the obtained effective moment matches perfectly the Pr^{3+} value. It should be mentioned that band structure calculations of $LaFe_4Sb_{12}$ support the possibility that Fe has a moment in this compound [90]. Assuming that the DOS of $PrFe_4Sb_{12}$ resembles that of $LaFe_4Sb_{12}$ the magnetic moment ascribed to (Fe_4Sb_{12}) comes from a double peak structure of the Fe-d partial DOS below the Fermi energy. On the other hand Tanaka et al. have shown that in a full filled $Pr_1Fe_4Sb_{12}$ sample a singlet ground state and no magnetic order should be present [91]. The appearance of Fe-moments may therefore be connected to vacancies in the RE-sublattice. To check this, in field Mössbauer measurements are a good method to contribute to this debate. Shenoy et al. [93] were the first who investigated a $LaFe_4P_{12}$ compound with Mössbauer spectroscopy in field. They concluded that a possible Fe moment has to be smaller than 0.01 μ_B. Therefore a larger survey of different Fe bearing skutterudites $A_xFe_4Pn_{12}$, with A equal to trivalent La, Pr, Nd, Eu, Yb, divalent Ca, Sr, Ba, and monovalent

Na, K, Tl most with Pn = Sb, but also some phosphorous based compounds was performed. Figure 8.28 shows the low temperature spectrum of two phosphorous based skutterutides $PrFe_4P_{12}$ and $NdFe_4P_{12}$ in zero field. The spectra can be fitted by only one doublet without any sign of line broadening. This is as expected, because in the structure only one crystallographic Fe site is present and X-ray diffraction have confirmed full occupation of the RE sublattice. In contrast for the antimony based RE compounds low temperature zero-field spectra are slightly asymmetric. This asymmetry is more pronounced in the spectra taken in external fields (Figs. 8.29 and 8.30). Because of the structure type, texture as reason for the asymmetry can be ruled out. Two subspectra are necessary to fit the spectra. Only the Yb sample needs only one subspectrum to fit the data satisfactorily well within the measuring accuracy, in agreement with the fact that Yb sublattice is fully occupied [95]. The intensities of the two subspectra is given in Table 8.2. Intensity of the majority subspectrum is within measuring accuracy in good agreement with the occupation number of the RE-atoms. Looking on the local surrounding of the Fe atoms there are 6 pnictogenic atoms forming the octahedron in the first shell and 12 Sb atoms in the next nearest shell together with two electropositive filler atoms (Fig. 8.31). The fact that especially in the RE sublattice the filling factor is smaller than 1, the Fe atom may have 0, 1 or 2 filler atoms in the second shell. The other Fe atoms are in a larger distance and may thus influence the central Fe atom only by a small amount. According to the filling factor x, probabilities concerning the frequency of the respective surrounding can be calculated by binomial distribution. E.g. for $x = 0.9$ probabilities of 0.81, 0.18, and 0.01 are obtained for the case to have 2, 1, or 0 RE atoms in the next nearest neighbour shell. Since the probability to have no filler atom in the next nearest neighbour shell is rather small, it can be added to the case to have 1 filler atom in this shell, thus giving an expected intensity ratio for the two subspectra of 81 to 19. The thus obtained values are in good agreement to the ones obtained from the Mössbauer fits (Table 8.2). A similar scenario was suggested for the Co based skutterudites $Tl_{0,8}Co_3FeSb_{12}$ and $Tl_{0,5}Co_{0,35}Fe_{0,5}Sb_{12}$ by Long et al. [96], but called into question, because of deviations of the observed area ratio of the subspectra from the ones calculated by statistical distribution. Above 4 T the spectra are fully polarized—visible by the vanishing of the $\Delta m = 0$ transitions (Figs. 8.28, 8.29 and 8.30). For the La and Yb compounds which show no magnetic order [76, 95] the values of the measured hyperfine fields B_{hf} for the subspectrum allocated to the component with the high intensity either coincide with the one of the applied field B_a, or were slightly larger. Significant deviations from the value of B_a were only obtained for Fe atoms allocated to the spectra with the small area. Similar behaviour is obtained for the Pr and Nd compounds, although according to bulk magnetic measurements they are magnetically ordered (ordering 5 K and 13 K for Pr [84] and Nd [76] (Fig. 8.27)). For the Eu compound an ordering temperature of 84 K is present [76, 77]. Calculated induced hyperfine fields $B_{ind} = B_{hf} - B_a$ are shown in Fig. 8.32. For the La, Pr, and Nd compounds B_{ind} exhibits some tendency towards saturation at high applied fields for the Fe site with the low intensity subspectrum, whereas for the Fe atoms allocated to the high intensity subspectrum B_{ind} scatters around zero (Fig. 8.32). For Yb the induced hyperfine field is within measuring accuracy also zero. In case of Eu

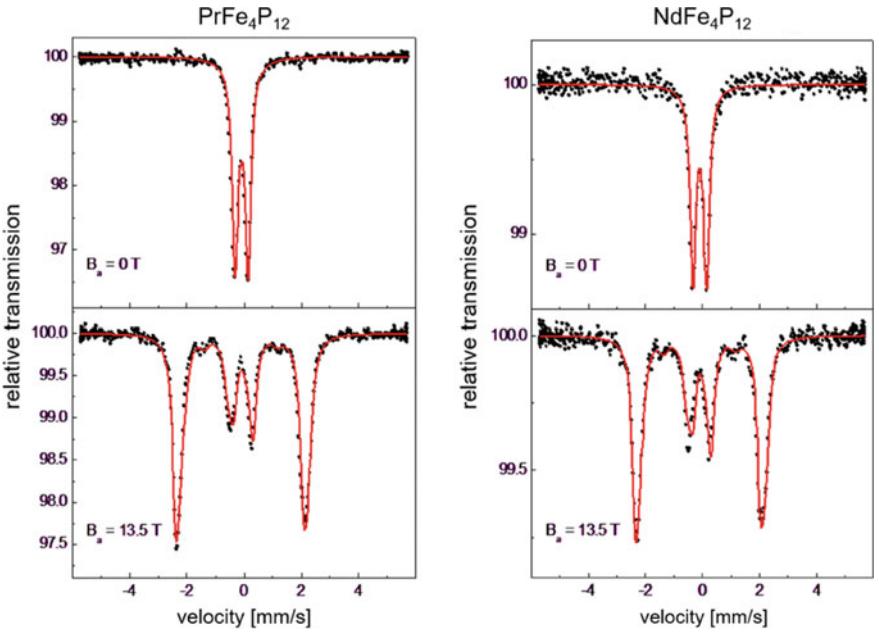

Fig. 8.28 Zero and high field spectra of $PrFe_4P_{12}$ (left) and $NdFe_4P_{12}$ (right) taken at 4.2 K

the induced hyperfine fields for both sites are negative. This indicates, that valence and core contribution to the hyperfine field are of comparable magnitude. If these contributions are of opposite sign and of similar magnitude, the measured hyperfine field can be rather small. As the magnetic moment is proportional only to the core contribution, such scenario can explain the small values of B_{ind} in comparison to the large effective moments obtained from magnetic measurements. This interpretation is strongly supported by ASW-FSM calculations [97, 98].

Changing now the trivalent RE filler atoms by monovalent Na, K, Tl and divalent Ca, Sr, Ba atoms, obtained spectra are very similar (Figs. 8.33 and 8.34). Again the spectra are asymmetric, demanding the use of at least two subspectra for interpretation of the measured spectra. The only one where one sub-spectrum is enough is the Ba compound (Fig. 8.33). An explanation for the second subspectrum in terms of voids in the filler subspectrum is in case of the di- and monovalent filler atoms not possible as the filling factor from chemical and X-ray analyses is in all cases higher than 98%, whereas the intensity of the second subspectrum is around 20%. However, with the exception of $TlCo_3FeSb_{12}$ [99] at present no experimental clue of theoretical hints exist for other interpretation of the difference in charge density at the Fe site in metallic skutterudites. For sub-stoichiometric Co-based skutterudites the existence of $CoSb_3$ gives the possiblility of another approach. A solid solution of a completely filled Fe compound in an unfilled Co compound was assumed to be realized in $Ce_xFe_{4-y}Co_ySb_{12}$ [100, 101].

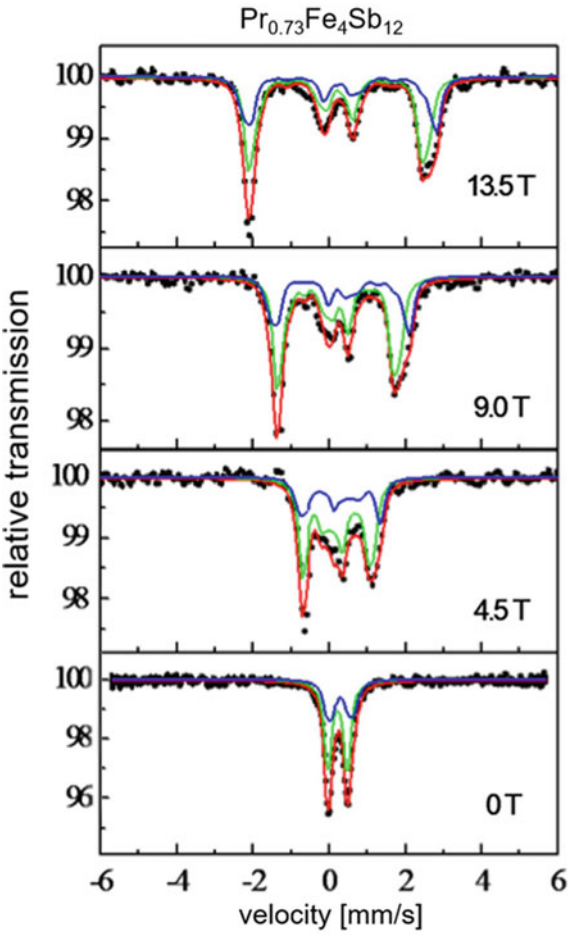

Fig. 8.29 Mössbauer spectra for $Pr_{0.73}Fe_4Sb_{12}$ at 4.2 K and different applied fields [92]. Reprinted from J. Mag. Mag. Matter, 272–276, M. Reissner, E. Bauer, W. Steiner, P. Rogl, High field Mössbauer and magnetic investigations of $Pr_{0.73}Fe_4Sb_{12}$, 813. Copyright (2004), with permission from Elsevier

The obtained induced hyperfine fields are similar to the ones for the RE skutterudites (Fig. 8.35). They all are less than 2 T. These values are too low to explain directly the effective moment assigned to the (Fe_4Sb_{12}) blocks from bulk magnetic measurements at high temperatures. Charge counting arguments that the moments on the (Fe_4Sb_{12}) blocks are due to the unpaired spins of Fe^{3+} in low spin configuration [76] are therefore wrong. The results support the picture of itinerant ferromagnetism with small ordered moments for the investigated di- and monovalent skutterudites. In summary, with the help of the in-field Mössbauer measurements it could be shown, that the magnetic structure is much more complex than expected from the simple crystallographic structure.

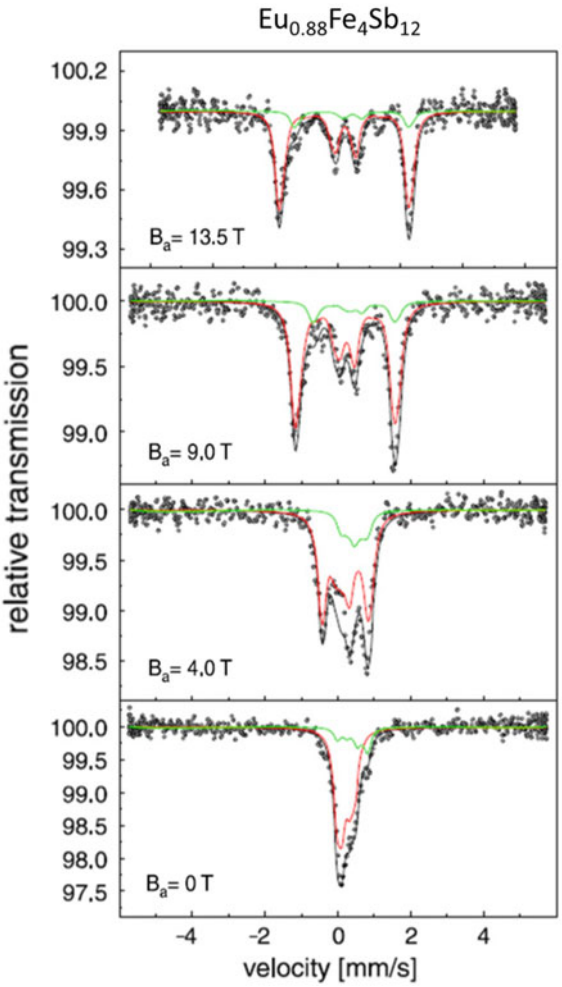

Fig. 8.30 Mössbauer spectra for $Eu_{0.88}Fe_4Sb_{12}$ 4.2 K and different applied fields [94]. Reprinted by permission from Springer: Hyperfine Interactions, Skutterudites, a thermoelectric material investigated by high field Mössbauer spectroscopy, M. Reissner, E. Bauer, W. Steiner, P. Rogl, A. Leithe-Jasper, Y. Grin, copyright (2008)

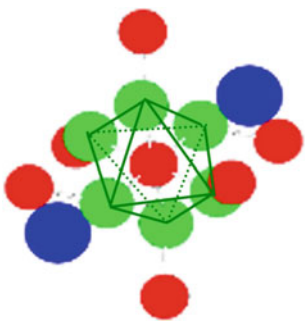

Fig. 8.31 Local surrounding of Fe atom. Large blue, medium green, and small red spheres denote A, Pn, and M atoms of AM_4Pn_{12}

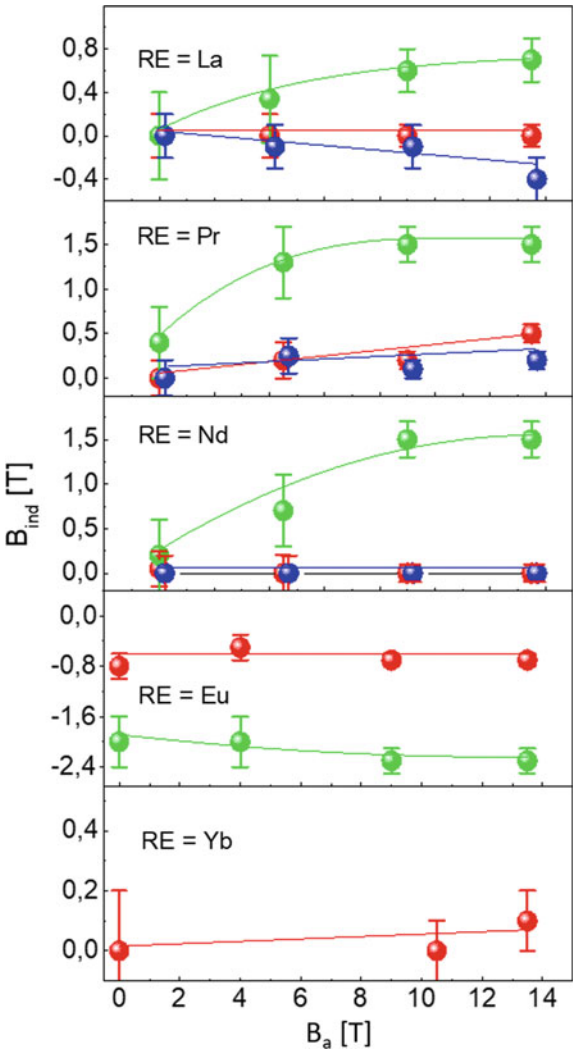

Fig. 8.32 Induced hyperfine field for $REFe_4X_{12}$ for X = Sb (red and green) and P (blue)

8.5.3 Spin Glasses

Spin glasses are mostly metallic alloys, showing magnetic, electronic and thermal anomalies below a characteristic temperature. Since the discovery of spin glasses in 1972 by Cannella and Mydosh [102] many good reviews and books have been published [103–107]. Spin glass behaviour was first found in noble metals with small amounts of impurities of transition metals, e.g. **Au**Fe, **Cu**Mn, and **Ag**Mn [102], but a lot of other materials turned out to show similar properties. Spin glasses are the paragon of disordered systems. There exists magnetic short range order which can

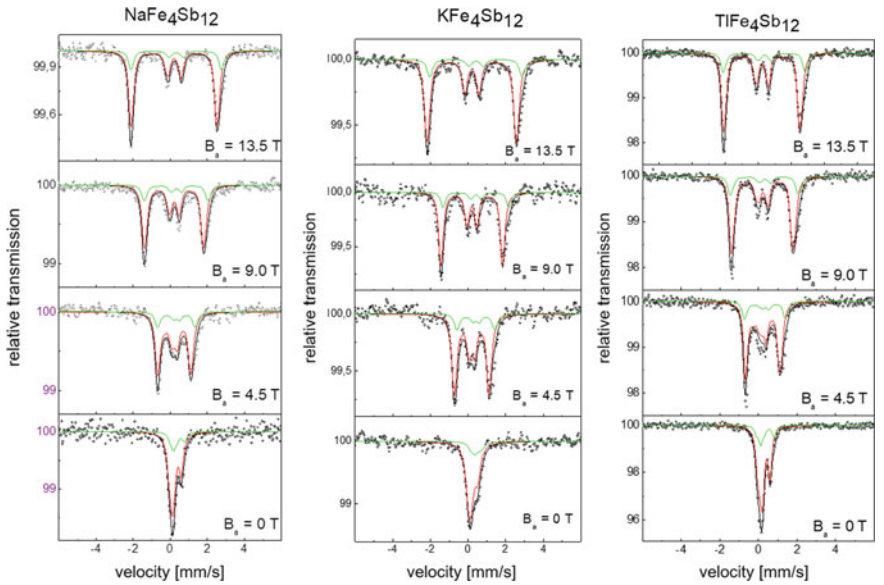

Fig. 8.33 Mössbauer spectra for monovalent filler atoms 4.2 K in different applied fields

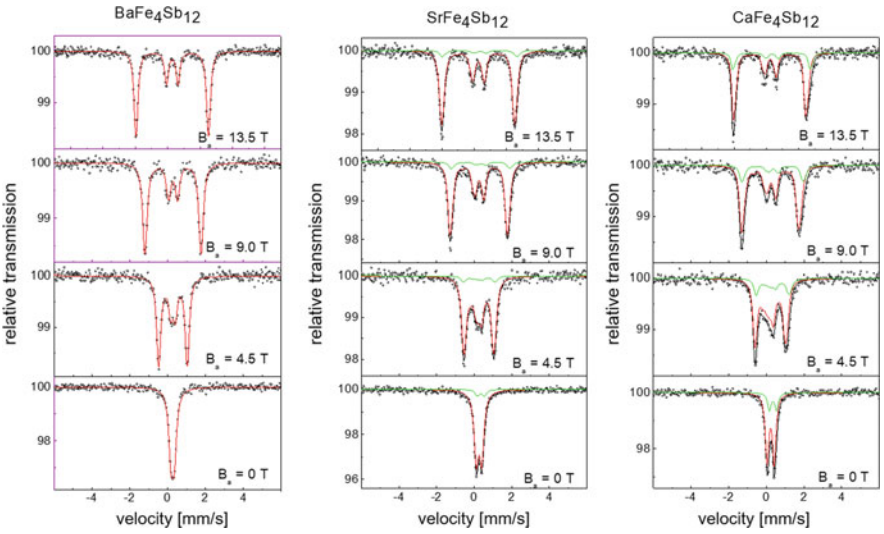

Fig. 8.34 Mössbauer spectra for divalent AFe_4Sb_{12} skutterudites for different fields at 4.2 K

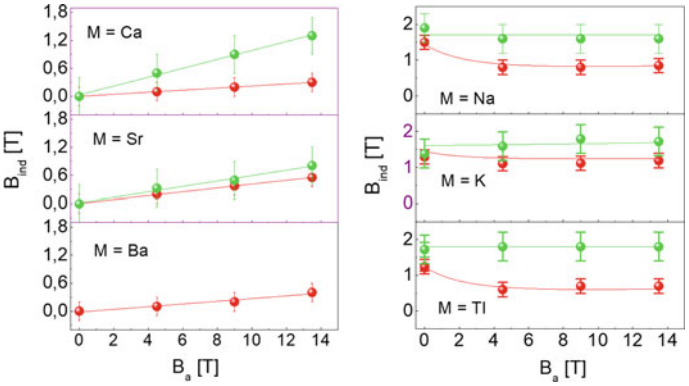

Fig. 8.35 Induced hyperfine fields for divalent (left) and monovalent (right) Fe-Sb skutterutides

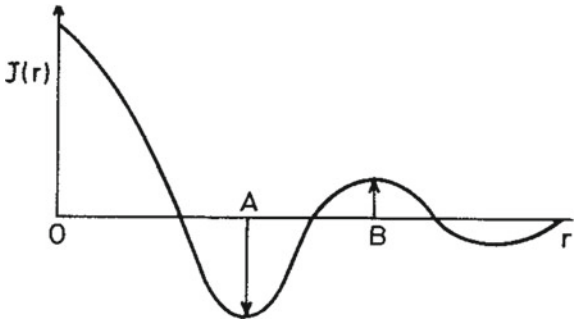

Fig. 8.36 RRKY interaction $J(r)$ between impurities at 0, A and B

be ferro- or antiferromagnetic. On the long range the order is inhomogeneous. In the above mentioned canonical or archetypical spin glasses [108] the reason for spin glass behaviour is the so-called RKKY [109–112] interaction, where the exchange integral J depends on distance r (Fig. 8.36). E.g. a spin at the origin 0 couples antiferromagnetic with spin A and less strongly ferromagnetic with spin B (Fig. 8.36). It is caused by an indirect exchange interaction of the local moments mediated by conduction electrons. Due to a random distribution of distances between moments, it is not possible to find a spin arrangement which fulfils all exchange interactions at the same time [113]. This is called frustration [103, 114]. A further class of spin glass materials are topological spin glasses, which can appear, if an antiferromagnetic arrangement of spins should be realized on a hexagonal lattice, where the basic geometric element is a triangle. One can arrange two spins antiparallel to one another on two of the corners of the triangle, but it is impossible to put a spin on the third corner which is antiparallel to both the others at the same time. This is also one kind of frustration. Because of the random distribution of the spins in the nonmagnetic matrix, which resembles the statistical distribution of atom positions in real glasses, Coles et al. [115] introduced the notation "spin glass" for this type of magnetism. Alternatively Paul Beck [116, 117] and Tustion and Beck [118] introduced

the name mictomagnet—from the greek syllabel *micto* for *mixed*—because of the simultaneous existence of ferro- and antiferro-magnetic correlations. At very low concentrations of magnetic impurity atoms, concentration independent scaling laws are present. When concentration increase, the possibility that two impurity atoms are nearest neighbours increases, and due to direct exchange interaction between d-orbitals magnetic clusters are formed. Such materials are called cluster glasses [115]. Cluster glasses are also possible due to chemical clusters, which may form during thermal treatment [116–118]. Moments of such clusters can have several thousand Bohr magnetons μ_B. If the density of the impurities is such, that the possibility that each impurity has at least one impurity in the nearest neighbour shell, the percolation limit is reached, where a path of neighbouring magnetic atoms goes from one side of the sample to the other. The probability that a moment is part of an infinite cluster is then larger than zero. The sample becomes long range ordered, but the order is strongly inhomogeneous. The main characteristic feature of spin glasses is the freezing of the moments in random orientations below a well defined freezing temperature T_f, without appearance of long range order. This freezing temperature was first discovered by a sharp peak in ac-susceptibility measurements [102] and later on confirmed also by dc-magnetization measurements [119–122]. For some spin glasses T_f is frequency dependent like for **Au**Fe and **Cu**Mn, whereas for others it is not. Below the freezing temperature strong irreversibilities are present in magnetization measurements, visible in large differences between field-cooled (FC) and zero-field cooled (ZFC) curves of temperature dependence of magnetization (Fig. 8.37). In this temperature regime also time dependence of magnetic moments is observed. Maxima are also present in specific heat and resistivity measurements, but not always at the same temperature as found in susceptibility measurements. Field dependence curves of magnetization $M(H)$ are strongly curved above T_f. They cannot be fitted by simple Brillouin function, but a fit assuming the existence of magnetic clusters of different size overlapped by a linear term from the single moments can explain the curvature $M(H,T) = \chi_0 H + \bar{\mu} c B(\bar{\mu}, (H + \lambda(M - \chi H))/T)$, with χ_0 a field independent susceptibility, $\bar{\mu}$ the mean moment with concentration c, λ the molecular field constant and B the Brillouin function. The fit shows that the mean moments of the clusters decrease with increasing temperature, whereas the number of clusters increase. This is a clear indication of dynamic magnetic behaviour. The existence of magnetic correlations above the ordering temperature is confirmed by specific heat measurements, which show that entropy at T_f is only 20 to 30% in case of Cu**Mn** [124] of the value expected in case of fully spin disorder in paramagnetic state. Under the first experiments proving a magnetic phase transition are Mössbauer experiments [125, 126], which have shown that below a temperature T_0 hyperfine splitting appears. The obtained hyperfine fields could be set in relation to local magnetic moments, with temperature dependence reminiscent to ferromagnetism. To determine, if the orientation of the spins is ferro- or antiferromagnetic, in-field Mössbauer spectra were performed on $Fe_{0,5}Au_{0,5}$ [127]. The result pointed to a weak canted antiferromagnet. Detailed analyses showed that hyperfine fields are statistical distributed in magnitude and orientation [128]. Whereas for **Au**Fe T_0 matches T_f obtained from susceptibility measurements, for other spin glasses like

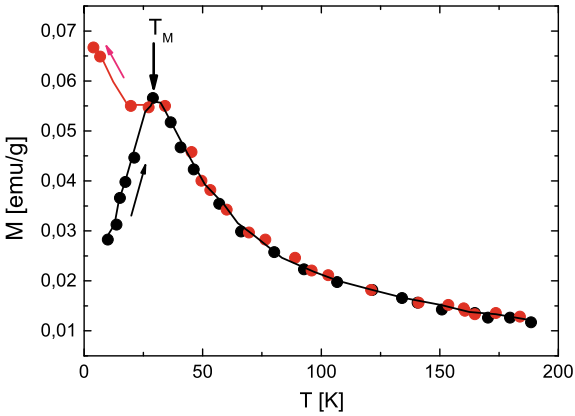

Fig. 8.37 Temperature dependence of the magnetization for $Y(Fe_{0.70}Al_{0.30})_2$ cooled without field to 4.2 K (black symbols) and with field (red symbols) [123]. © IOP Publishing. Reproduced with permission. All rights reserved

CuMn T_0 is higher than T_f. Further, small hyperfine fields are also present above T_0, proving that magnetic correlations are present above the ordering temperature [129, 130]. From small angle neutron measurements on **Au**Fe a maximum in temperature dependence of the neutron scattering cross section was found which is strongly q-dependent. Compared to susceptibility measurements T_0 is sometimes more than 10 K higher than T_f (e.g. [131]).

Very soon it was clear that the very sharp cusp in susceptibility measurements could not be explained by simple mixing of ferro- and antiferro-magnetic phases. Thus a lot of efforts were undertaken to theoretically explain these new type of magnetic behaviour. One of the first were Edwards and Anderson [132], who proposed a new ground state in which all spins are frozen in random directions below a well defined temperature. The order parameter is the autocorrelation function $q(t) = [< S_i(0)S_i(t) >_T]_{conf}$ which measure the probability that a spin has, after some time, still the same orientation. The outer bracket represents the configurational and the inner bracket the thermal average. Therefore q equals 1 in the ordered state at $T = 0$ and q becomes 0 above the ordering temperature. To calculate the free energy the Hamiltonian is build up in such a way that the spins are arranged on a regular lattice and the exchange interactions are randomly distributed. Within this model neither the cusp in susceptibility can be well reproduced, nor does the obtained specific heat agree with experiment. Subsequently many new theories based on the Edwards-Anderson model have been developed. Sherrington and Kirkpatrick [133] put this mean-field theory on quantum mechanical ground. Soukolis and Levin [134] introduced clusters and took into account both intra- and intercluster interactions. Intracluster interactions are strong and calculated exactly, whereas the weak intercluster interactions are treated in a mean field approximation. Results fit well to experimental findings. Intercluster interactions lead to the sharp peak in susceptibility and intracluster interactions lead to the smooth maximum observed in specific heat. Very interesting is the outcome of the Replica Symmetry Breaking model of Parisi [135] which proposes a multi-valley free energy landscape in the configuration

space. The system can jump between different spin configurations by overcoming the barriers between the valleys. Due to the different heights of the separating barriers, different relaxation times are present. This leads to dynamic behaviour. A hierarchical distribution of time scales should be present, which could explain the experimentally observed relaxation behaviour and irreversibilities. All the theories based on the Edwards-Anderson model assume a thermodynamic phase transition into a ground state. In such case the transition temperature should be independent from experiment always the same. This is in contradiction to many experiments and also to the fact that above the ordering temperature the expected pure paramagnetism is not present, but lots of magnetic correlations are verified to exist up to temperatures several times higher than T_f. In 1974 Tholence and Tournier [136] and later Wohlfarth [137] proposed that the spin glass transition is not a true thermodynamic phase transition, but is very similar to blocking of single domain particles in rock materials. For this Néel has developed the theory of superparamagnetism. A short range order couples the spins into clusters. Because temperature counteracts the formation of such clusters, the size of the clusters increases with decreasing temperature. At high temperatures the clusters are free to rotate. They jump between easy axis directions, which are separated by energy barriers caused by anisotropy effects. This can be described in the Néel theory by τ_0, an intrinsic relaxation time in the range of $\sim 10^{-9} s$ and $E_a = KV$ the anisotropy energy with K the anisotropy constant and V the particle volume. For a particular measurement, which is characterized by a typical measuring time τ_m, clusters appear frozen, if their relaxation time τ is longer than τ_m. With decreasing temperature, volume of clusters increase and therefore the rotation frequencies decrease, and at a distinct temperature the clusters become blocked. In case of a cluster size distribution, clusters of different size will block at different temperatures. Coming from high temperatures the largest cluster will be blocked first. Within this picture the measured zero-field cooled and field-cooled curves (Fig. 8.37) are well understood. At high temperatures all clusters are free to rotate. All τ values are shorter than τ_m and the measured magnetization is zero. In lowering the temperature the cluster gradually freeze in random directions. Thus at low temperature the measured magnetization is still zero. In applying a small measuring field and by increasing the temperature (ZFC curve) the magnetization increases, because—starting with the smallest ones—more and more clusters are freed, due to the thermal energy kT and rotate in direction of the applied field. The increase of magnetization stops when the largest clusters are rotated in direction of the applied field. With further increase of temperature the thermal energy destroys successively the alignment and magnetic signal decreases like in a paramagnet thus forming the observed cusp. If temperature now decreases (FC curve), due to reduction of thermal energy, clusters begin again to rotate in direction of applied field, starting with the smallest ones and ending with the largest ones. Magnetization increases until it reaches maximum again. With further decrease of temperature the magnetization stays constant, because all clusters are now frozen in direction of the applied field. Therefore the temperature where the cusp appears is called the freezing temperature T_f. In this model all the irreversibilities and time dependences obtained in experiment can be explained. It also explains, why the value T_f is different for different measuring

methods. With decreasing characteristic measuring time freezing temperature should increase. This illustrates why T_f for magnetization measurements ($\tau_m \sim 1 - 10^{-4}$ s) is smaller than for Mössbauer measurements ($\tau_m \sim 10^{-9}$ s) and much smaller for neutron measurements ($\tau_m \sim 10^{-9} - 10^{-12}$ s). Further, in this model it is clear that magnetic correlations are present far above the freezing temperature. Only at much higher temperatures, when the short range order of the clusters is destroyed, pure paramagnetic behaviour is found. Mössbauer spectroscopy in external magnetic field is an excellent method to investigate the magnetic dynamics above the freezing temperature, because the applied field changes the relaxation frequency of the clusters. If fields are large enough, they can shift the characteristic time of the dynamics into the Mössbauer time window, so that the approximation of fast relaxation limit is no longer fulfilled and the spectra show typical shape of so-called relaxation spectra. This will be shown exemplarily in the following for the spin-glass-system Y(Fe, $Al)_2$.

8.5.4 Y(Fe, Al)$_2$

$Y(Fe_xAl_{1-x})_2$ is a Laves phase, which crystallizes, with the exception of a small region near $x = 0.5$, in the cubic $MgCu_2$ structure type. Whereas YAl_2 is a Pauli paramagnet with a nearly temperature independent susceptibility of $0.8 \cdot 10^{-6}$ emu/g at room temperature, YFe_2 is a ferrimagnet with an Fe moment of $1.77 \pm 0.08\mu_B$ and a strongly delocalized yttrium moment of $-0.67 \pm 0.04\mu_B$ [63, 138]. For $x \geq 0.78$ reciprocal susceptibility χ^{-1} data are linear in temperature following a Curie-Weiss law (Fig. 8.38 right). For lower iron concentrations x the $\chi^{-1}(T)$ data are strongly curved (Fig. 8.38 left). They could be fitted by the relation $\chi = \chi_0 + C/(T - \Theta)$ where χ_0 describes the Pauli paramagnetic matrix contribution. The Weiss temperature Θ scatters around zero on the Al-rich side and increase strongly on the Fe rich side (Inset Fig. 8.39). From the Curie constant C the mean effective moment $\mu_{eff} = g\mu_B\sqrt{S(S+1)}$ is obtained, which is nearly concentration independent. Above $x \geq 0.78$ it is nearly constant equal to the value obtained for YFe_2 (3.02 μ_B) [139, 140] in contrast to the spontaneous moment which strongly decreases (Fig. 8.39). On the Al-rich side it decreases slightly to below 2 μ_B/Fe for $x = 0.1$ [123]. Although no long range magnetic order could be found down to 30 mK even at 70% Fe, the magnetization curves on the Al-rich side are still strongly curved. They could be fitted to $M = N\bar{\mu}L(\bar{\mu}H/kT) + \chi H$, with L the Langevin function. The first term describes the magnetization of iron atoms gathered in clusters with the mean cluster moment $\bar{\mu}$ and N the number of mean clusters. The second term is a susceptibility term coming from the moments which are not part of a cluster. Calculation gives mean cluster sizes of 3–4 magnetic atoms. Their concentration is a few percent. This finding is confirmed by diffuse neutron scattering on two compounds with $x = 0.25$ and 0.65, where the magnetic scattering was interpreted as arising from small clusters of less than 10 Å at temperatures far above the freezing temperature [142]. These clusters are formed by short range ferromagnetic correlations. There is

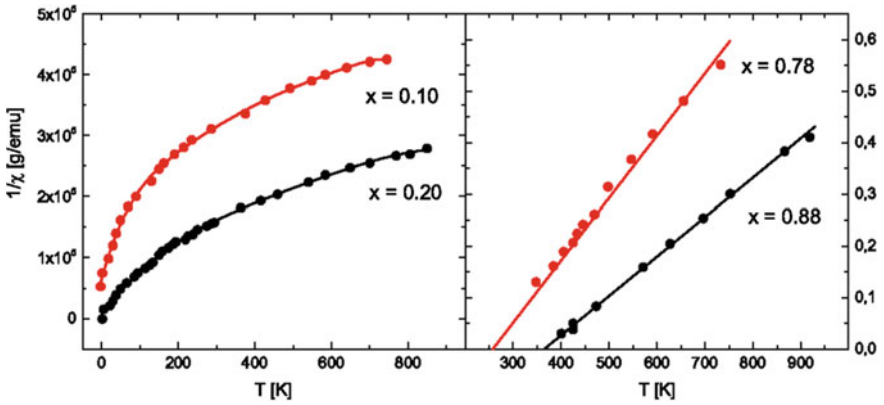

Fig. 8.38 Temperature dependence of the reciprocal susceptibility for several typical samples of $Y(Fe_xAl_{1-x})_2$ [123]. © IOP Publishing. Reproduced with permission. All rights reserved

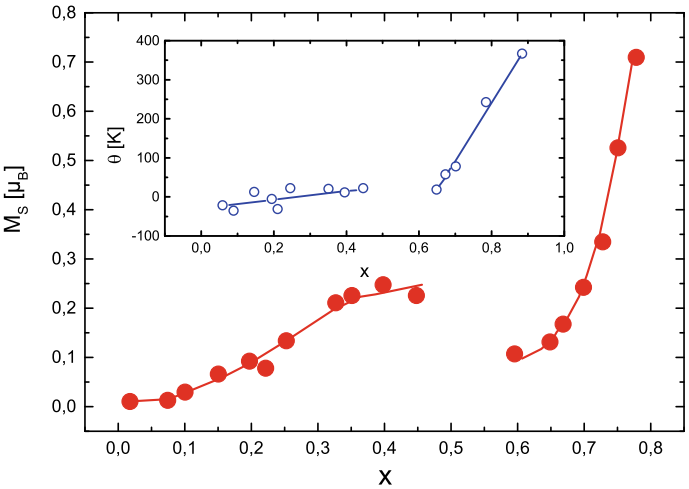

Fig. 8.39 Concentration dependence of the saturation moment $M_s = N\mu$ for $Y(Fe_xAl_{1-x})_2$ at 4.2 K. Inset: concentration dependence of Weiss temperature θ [123]. © IOP Publishing. Reproduced with permission. All rights reserved

also some evidence of weak antiferromagnetic correlations. From the nuclear diffuse scattering indication of a weak anticlustering of Fe on Al sites is found [142]. The low-field magnetization against temperature curves show maxima (T_M) for $x \leq 0.8$, which broadens with increasing x.

Zero-field ^{57}Fe Mössbauer spectra at room temperature are strongly asymmetric (Fig. 8.40). They can be fitted by a superposition of quadrupole split spectra. The change of asymmetry with x points to a strong influence of the local surrounding on the electrostatic hyperfine interactions. At low temperature magnetic hyperfine split-

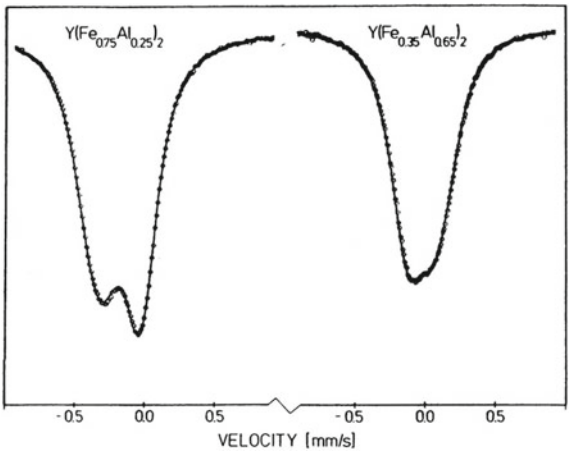

Fig. 8.40 Room temperature ^{57}Fe Mössbauer spectra of typical $Y(Fe,Al)_2$ samples [141]. Reprinted by permission from Springer: Hyperfine Interactions, Electrostatic hyperfine interactions $Y(fe, Al)_2$, M. Reissner, W. Steiner, copyright (1986)

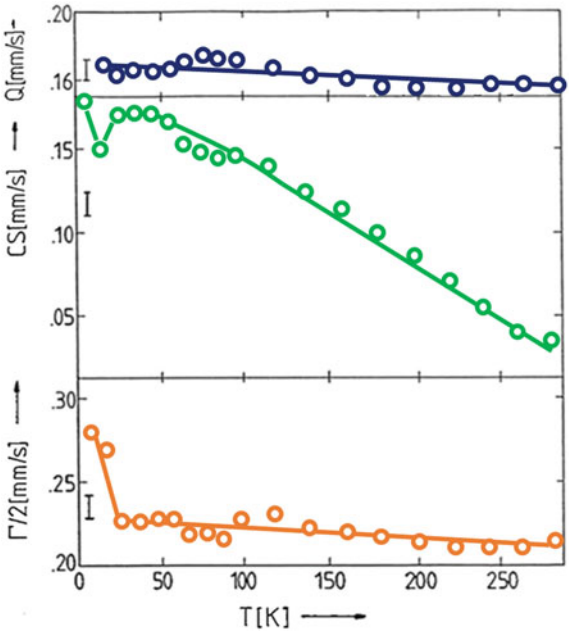

Fig. 8.41 Temperature dependence of the mean quadrupole splitting Q, mean centre shift CS (rel. ^{57}CoRh) and half width Γ/2 of $Y(Fe_{0.4}Al_{0.6})_2$. Adapted from [143]

ting is present. The transition temperature T_A, where magnetic hyperfine splitting appears, is well defined by a strong increase of half width, if spectra are still fitted by superposition of quadrupole split spectra (Fig. 8.41). T_A is in good agreement with the ordering temperature T_c obtained from the magnetic measurements on the Fe-rich side, whereas it is slightly higher than T_M on the Al-rich side, which is as mentioned above typical for spin glass behaviour and caused by the different time scales of the experiments (Fig. 8.42). The range above the ordering temperature where non-linear

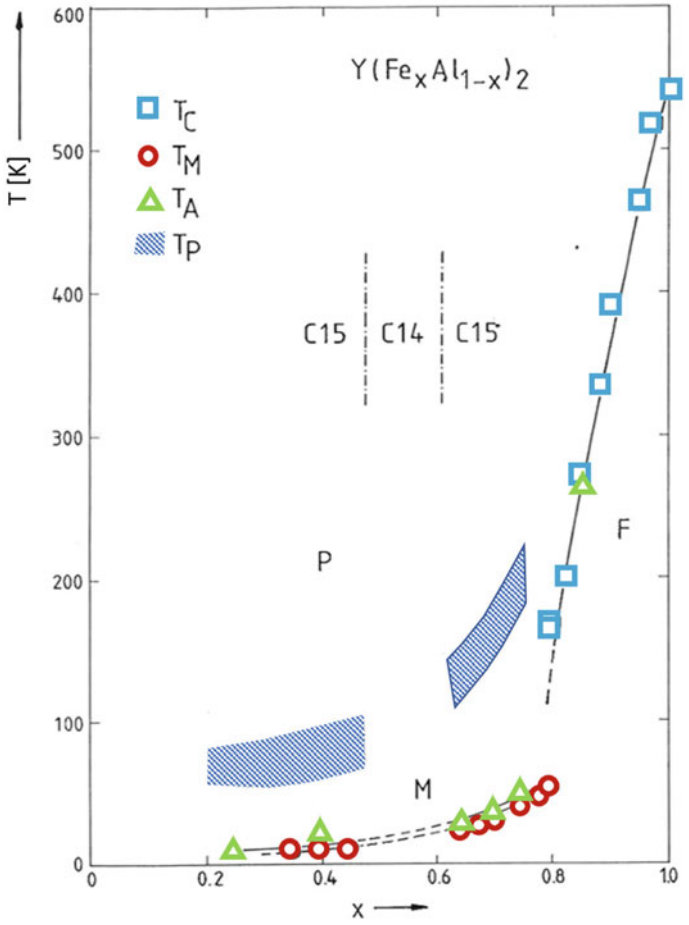

Fig. 8.42 Magnetic phase diagram of $Y(Fe_xAl_{1-x})_2$, T_c Curie temperature, T_M maximum temperature, T_A temperature where magnetic hyperfine splitting vanishes, T_P temperature above which magnetization curves are linear. Adapted from [143]

magnetization curves are still present, extends to 7 times T_f. Below T_M irreversibilities, time dependence and history effects are present. This all indicates cluster glass behaviour for $x < 0.78$. One point left open by these investigations is the question concerning the stability of the Fe moment. The only mildly concentration dependent mean effective moment points to a non-vanishing Fe moment that stays relatively constant over the entire concentration range, whereas the Mössbauer investigations indicate a strong influence of local environment on electrostatic and magnetic hyperfine interactions. Therefore the question arise, whether or not the iron moment also depends on the local coordination. There were some contradicting results in literature. Non spin-polarized band-structure calculations on $Y(Fe,Al)_2$ have shown a

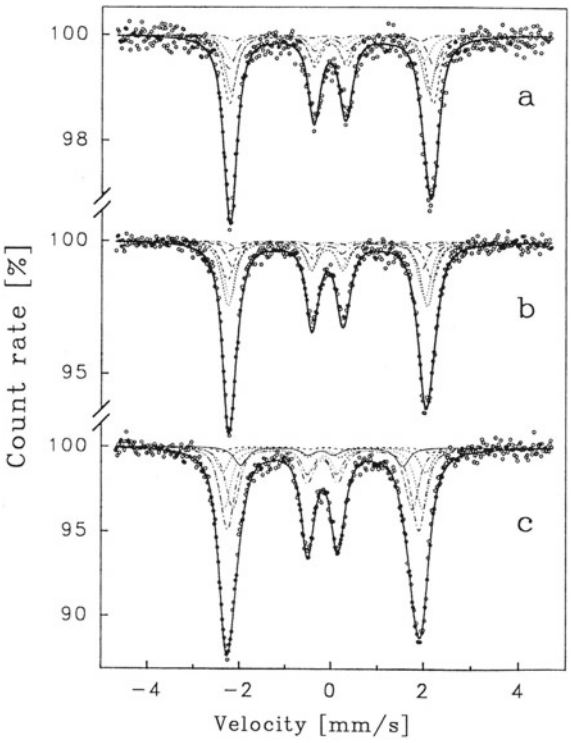

Fig. 8.43 ^{57}Fe transmission Mössbauer spectra of $Y(Fe_xAl_{1-x})_2$ at room temperature and $B_a = 13.5$ T for **a** $x = 0.25$, **b** $x = 0.40$, and **c** $x = 0.65$ [150].

reduction in the density of states at low iron concentrations [144, 145]. For Fe in Al non-magnetic Fe atoms were found from experiment [146, 147], whereas first-principle calculations [148, 149] predict an iron moment of 1.7 μ_B. Further it is shown, that in these compounds the Fe moment strongly depend on lattice constant.

To get more information about the stability and environment dependence of the iron moment in $Y(Fe_xAl_{1-x})_2$ in the paramagnetic regime, high field Mössbauer measurements were performed and compared with results of spin-polarized band-structure calculations [150]. Four representative samples with x = 0.25, 0.40, 0.65, and 0.75 were chosen. The Mössbauer measurements were performed at external fields up 13.5 T in temperature range 50–300 K, 100–300 K, 160–300 K, and 280–300 K for the four samples. Within these temperature ranges the respective magnetization curves are straight lines, indicating that short-range order effects are vanished. The Mössbauer spectra taken in applied fields B_a are all magnetically split (Fig. 8.43) with hyperfine fields aligned parallel to the applied field, indicated by the vanishing of the second and fifth line ($\Delta m = 0$). The spectra are asymmetric with deeper and narrower lines on the low velocity side. Therefore several subspectra are necessary to fit them. Crystallographically only one Fe/Al site exists, where Fe is surrounded by 6 Fe/Al nearest and 12 Y next nearest neighbours. Therefore a maximum of 7 subspectra, representing 0, 1, 2, 3, 4, 5, or 6 Fe atoms in the first neighbour shell, are

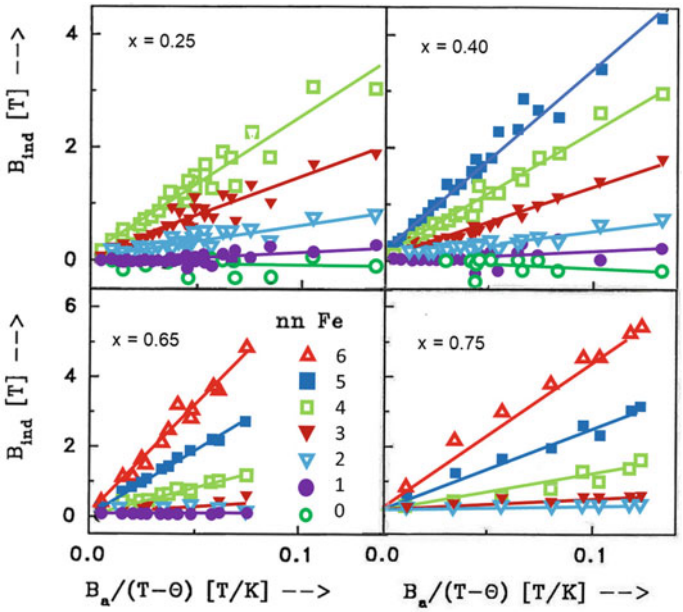

Fig. 8.44 Dependence of induced hyperfine fields in $Y(Fe_xAl_{1-x})_2$ on $B_a/(T-\theta)$ for $x = 0.25$, $x = 0.40$, $x = 0.65$, and $x = 0.75$ [150].

expected to be adequate to fit the measured spectra. From the thus obtain hyperfine fields B_{hf} the induced hyperfine fields B_{ind} can be deduced from $B_{ind} = B_a$-B_{hf}. Obtained B_{ind} values increase with increasing number of iron nearest neighbours (Fig. 8.44). From these data a Mössbauer Curie constant C_{ind}^{MB} can be calculated according to a Curie-Weiss law from $B_{ind}/B_a = C_{ind}^{MB}/(T\text{-}\Theta)$. For Θ, values obtained from the analyses of the magnetic measurements (Inset Fig. 8.39) are taken. C_{ind}^{MB} is strongly different for different Fe-surroundings. It slightly decrease with increasing iron concentration x, whereas the mean value increases with x. For zero or one Fe atom in nearest neighbour shell C_{ind}^{MB} is near to zero. Assuming, as often done and working well in many systems e.g. Fe-B alloys [151], a direct proportionality between induced hyperfine field and magnetic moment, this small C_{ind}^{MB} values would indicate vanishing Fe moments at least for zero and one Fe nearest neightbour shells, which is in full contradiction to the high, only slightly concentration dependent effective moments obtained from the magnetic measurements. LAPW and ASW band-structure calculations gave iron moments of 1.98 μ_B, 1.57 μ_B, and 1.93 μ_B for YFe_2, Y_2Fe_3Al, and Y_2FeAl_3. They also confirmed that Y carry a small moment, which is antiparallel to the Fe moments and decreases with Al concentration from $-0.42\mu_B$ for YFe_2 to $-0.31\mu_B$ for Y_2Fe_3Al and $-0.08\mu_B$ for Y_2FeAl_3. This shows that a calculation of the effective Fe moment from magnetic measurements by ignoring the Y moment leads to underestimated μ_{eff} values on the Fe side, but to more

precise μ_{eff} values on the Al-rich side. Theoretically calculated hyperfine fields B_{tot}^{th} consist of two contributions: a nearly concentration independent contribution from the 3d electrons B_{core}^{th} and one from the valence electrons (4s and 4p) B_{val}^{th} which increases linearly with decreasing Fe content and has opposite sign (Fig. 8.45). For YFe_2 B_{val}^{th} is small and total hyperfine field is direct proportional to the Fe moment as usually assumed [151]. Surprisingly, with increasing Al concentration the valence electrons are strongly positive polarized. By varying the used lattice constant for the calculations allows to estimate the volume dependence of the theoretical hyperfine field. E.g. calculation of Y_2Fe_3Al with the measured lattice constant of YFe_2 (7.36 Å) instead of 7.48 Å corresponds to a concentration change from $x = 0.75$ to $x = 1.0$. This calculated concentration dependence of theoretical hyperfine fields is shown as short solid lines in Fig. 8.45. Their slopes are nearly independent of x and cannot be the reason for the concentration dependence of the hyperfine fields. The negative slope of the volume dependence of B_{tot}^{th} explains the decrease of experimentally obtained Curie constant B_{ind}^{MB} with x for fixed number of nearest neighbour Fe atoms. Because the theoretical calculations are done on ordered compounds with experimentally obtained lattice constants, the results can only describe one of the different Fe surroundings used in the Mössbauer analysis. Nevertheless B_{tot}^{th} shows the same trend on number of Fe nearest neighbours as the experimentally obtained Curie constant C_{ind}^{MB}. To get now local susceptibilities, the experimentally obtained induced hyperfine fields have to be decomposed into the core contribution B_{core} and the valence contribution B_{val}. The local susceptibility is only related to B_{core}, which can be compared with the local Fe moment, which originates from the 3d electrons. Because both B_{ind}/B_a and the susceptibility χ^{mag} determined from the magnetic measurements follow a Curie-Weiss law, one can assume that B_{core} also follows such behaviour namely $B_{core}/B_a = C_{core}^{MB}/(T\text{-}\theta)$. As a consequence B_{val}/B_a must also follow a Curie-Weiss law. With help of the band-structure calculations a separation of B_{core} and B_{val} is possible. Since the theoretical valence contribution decreases linearly with x to nearly zero for YFe_2 (Fig. 8.45), similar linear behaviour is assumed for the valence contribution of the experimentally obtained mean Curie constant $\bar{C}_{val}^{MB}$. To determine the slope of the concentration dependence of $\bar{C}_{val}^{MB}$, one assumes that the core part of the mean Curie constant obtained from Mössbauer measurements $\bar{C}_{core}^{MB}$ is directly proportional to the magnetically determined Curie constant C_{mag}. Relating C_{mag} to one Fe atom shows that both mean $\bar{C}_{core}^{MB}$ and mean $\bar{C}_{mag}$/Fe are linearly increasing with x (Fig. 8.46), indicating that the direct proportionality between mean $\bar{C}_{core}^{MB}$ and mean C_{mag} is consistent with the data. There is only one hyperfine coupling constant relating B_{ind} to μ_{Fe} for all x. The concentration dependence of the core contribution of the induced hyperfine field, determined from the Mössbauer investigations, is in perfect agreement with the concentration dependence of the effective moment, determined from the bulk magnetic measurements. If one now assumes that the valence contribution of the Curie constant for each Fe surrounding is linear, the values C_{val}^{MB} and C_{core}^{MB} for the individual Fe environments can be calculated from the respective measured induced hyperfine fields B_{ind} in the same way as was just done for the mean $\bar{C}_{val}^{MB}$ values. The local susceptibilities are now given by $\chi_{loc} = B_{core}/B_a$ with $B_{core} = C_{core}^{MB} B_a/(T - \theta)$ (Inset Fig. 8.46). For

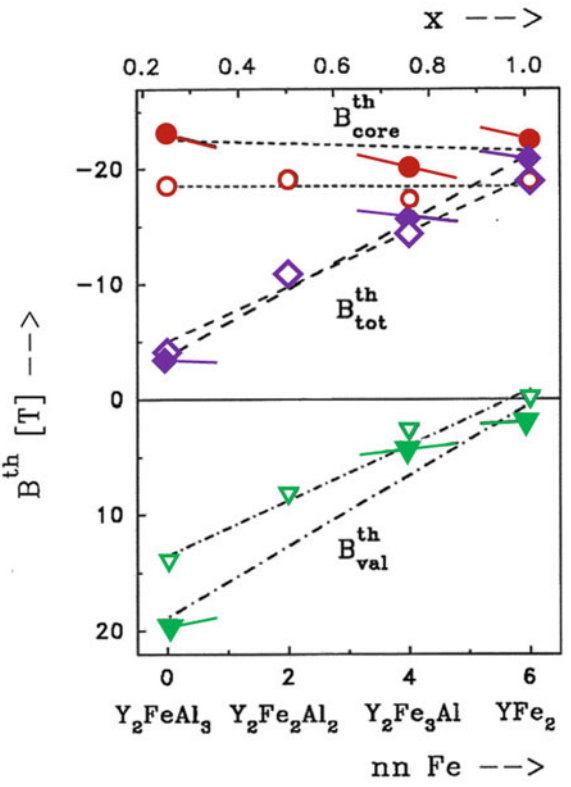

Fig. 8.45 Calculated (open symbols ASW, full symbols LAPW) hyperfine fields $B^{th}_{core}(\circ)$, $B^{th}_{tot}(\diamond)$ and $B^{th}_{val}(\triangledown)$ for $Y(Fe_xAl_{1-x})_2$ [150]. © IOP Publishing. Reproduced with permission. All rights reserved

up to three nearest Fe neighbours C^{MB}_{core} values are constant. For higher iron concentration in the nearest neighbour shell an increase is present. From this it can be concluded that Fe carries a moment even if surrounded only by Al atoms, in agreement with the band-structure calculations (Fig. 8.45). The increase of χ_{loc} for the Fe rich surroundings reflects the increase of the mean Curie constant $\bar{C}^{MB}_{core}$ and of μ_{eff}. In summary, from magnetization and high field Mössbauer measurements and with the help of band-structure calculations it could be proved that all iron atoms carry a magnetic moment in the paramagnetic regime of the $Y(Fe_xAl_{1-x})_2$ cluster glass.

Entering now the temperature regime $T_f < T <\sim 7 \cdot T_f$, where magnetic correlations are present, visible in the bended magnetization curves, the Mössbauer spectra in applied magnetic field change drastically their shape. Figure 8.47 shows spectra for $x = 0.75$ at $1.8 \cdot T_f$ (left) and $5 \cdot T_f$ (right). The shape of the spectra at 13.5 T are quite different from those obtained at room temperature in the pure paramagnetic region (Fig. 8.43). The spectra can no longer be fitted by a superposition of subspectra with intensities according to the different iron environments, calculated by binomial distribution. The nearer the temperature to T_f, the more is the deviation in shape from the one for the paramagnetic case. Often spectra with similar shape are analysed by distribution of static hyperfine fields [152, 153]. Figure 8.48 gives

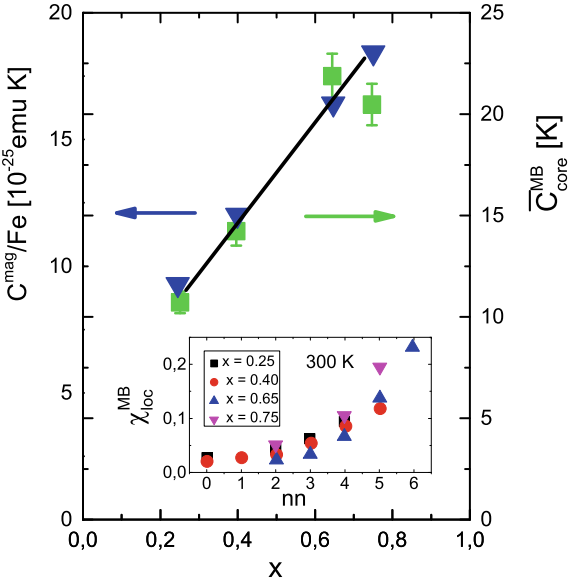

Fig. 8.46 Comparison of the x dependence of C^{mag} per Fe atom from magnetization measurements (full triangle down, left-hand scale) with that of $\bar{C}^{MB}_{core}$ from Mössbauer measurements (full squares). Inset: Dependence of local susceptibility χ^{MB}_{loc} on number of nearest Fe neighbours in $Y(Fe_xAl_{1-x})_2$ at 300 K; $x = 0.25$ (full square), 0.40 (full circle), 0.65 (full triangle up) and 0.75 (full triangle down) [150]. © IOP Publishing. Reproduced with permission. All rights reserved

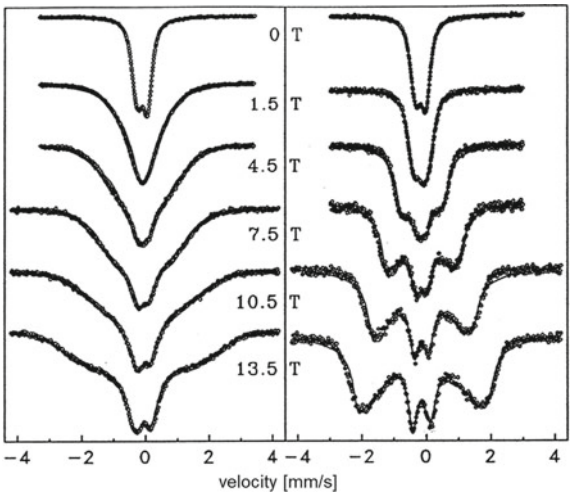

Fig. 8.47 Spectra of $Y(Fe_{0.75}Al_{25})_2$ in different fields at 70 K (left) and 200 K (right). Fits according to described model. Reprinted from [154]

an example of a fit in the fast relaxation limit with 9 subspectra according to a hyperfine field distribution. The structure in the calculated spectrum is not visible in the measured one, and could be avoided by increasing the number of subspectra. The fit is reasonable, but there is no meaningful interpretation, because the subspectra with the largest magnetic hyperfine splitting have hyperfine fields larger than the applied field. Because all spectra are fully polarized, it has to be concluded, that there are contributions to the hyperfine field which are parallel to the applied field B_a. This would imply magnetic moments which are antiparallel to B_a, a scenario not very

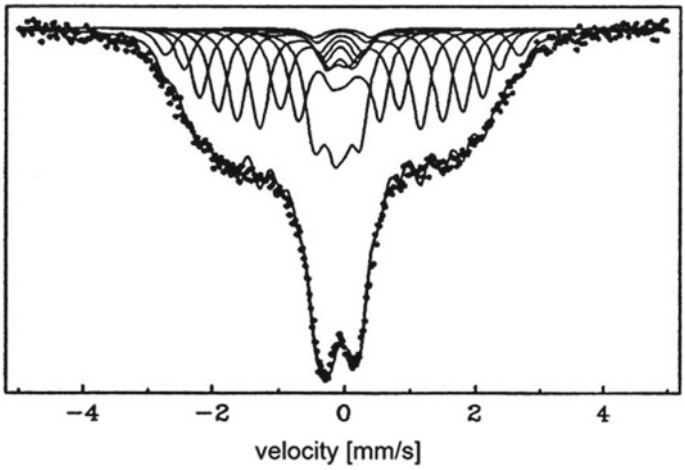

Fig. 8.48 Spectrum of $Y(Fe_{0.75}Al_{0.25})_2$ at 100 K and 13.5 T analysed in approximation of fast relaxation by hyperfine field distribution. Reprinted from [155]

plausible. On the other hand the usual case, that iron moments are parallel to the applied field would give internal hyperfine fields higher than 27 T, which is larger than the ones for undiluted YFe_2 (two subspectra 21.2 T and 20.8 T [156, 157]) and taking into account that, as mentioned before, for the shown high Fe concentration ($x = 0.75$) only core contributions to the hyperfine field are important, also too high magnetic moments would be the consequence. From the shape of the spectra, smooth inner slope of the outer lines and strongly increased intensity in the inner part of the spectra like for relaxation spectra, the dynamics of the magnetic correlations seems to be visible. Figure 8.49 shows spectra at 100 K and 13.5 T for different Fe concentration x. Here 100 K corresponds to 10, 4, and 2.5 times T_f for $x = 0.40$, 0.65, and 0.75, respectively.

The simplest model to describe dynamics is a field flip model where two magnetic hyperfine fields H_1 and H_2, which are antiparallel to one another, fluctuate between two states $|1>$ and $|2>$. If W_i is the equilibrium occupation of state $|i>$, and transition probability between the states is γ_{12} and γ_{21}, the equilibrium condition gives $W_1\gamma_{12} = W_2\gamma_{21}$. The iron nucleus senses a field jumping between B_1 and B_2. The relaxation rate is then given by $\tau = 1/(\gamma_{12} + \gamma_{21})$. The asymmetry of the spectra found in the zero field spectra (Fig. 8.40), which is due to different quadrupole splitting and centre shift according to the different iron surroundings, is also visible in the in-field spectra, and should be taken into account also in the dynamical fits. To avoid this necessity, spectra at higher fields should be preferably analysed, because at the high fields the electrostatic hyperfine interaction is much smaller than the magnetic one. The result of such simple fit, which takes into account only two subspectra, is for many temperatures reasonable (Fig. 8.50). For the occupation probability of the two states, a Boltzmann statistics was chosen with $\tau_{on}/\tau_{off} = exp(\mu_B g(B_o - B_u)/kT)$, with g set to 1. In principle the results seem to favour such field flip model. But

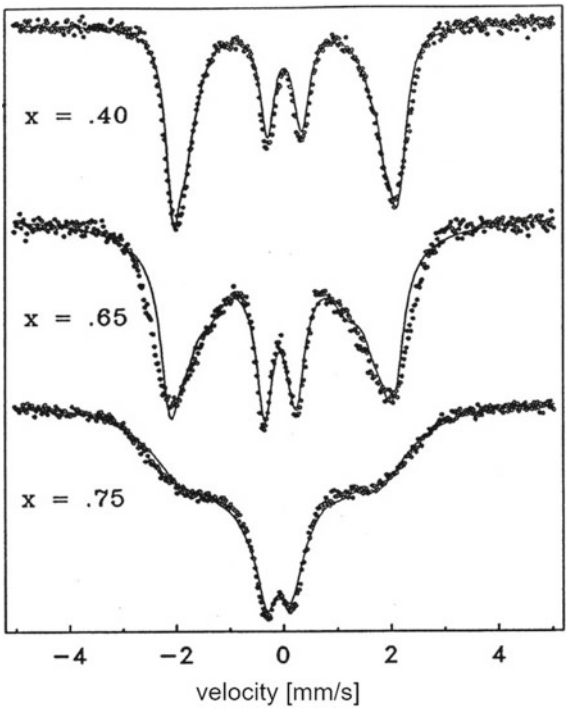

Fig. 8.49 Spectra of $Y(Fe_xAl_{1-x})_2$ at 13.5 T and 100 K for different x. Reprinted from [19]

the values of the obtained fields $B_o = B_a + B_{cl}$ and $B_u = B_a - B_{cl}$, where B_{cl} is the hyperfine field of iron moments in the correlated state, that means in a magnetic cluster, between which the hyperfine field flips, give no constant B_{cl} value (Fig. 8.51). Further the value of B_u needed to fit the inner part of the spectra—with $B_{cl} \sim 8$ T—leads to contributions resulting for B_o that are not present in the measured spectra. Therefore a different more complex model for the dynamics in these compounds is necessary. Usually the short range order, found in spin glasses above T_f is explained by a growth of size of clusters with decreasing temperature and their changing rotation frequency. What is neglected in this picture is the possibility of real dynamics, which is suggested by the shape of the Mössbauer spectra. Due to the high applied magnetic field B_a the dynamics of the clusters above T_f, which is too fast to be seen in the zero-field measurements, become visible. The mean life time of a correlated state, which results in effective magnetic moments oriented in direction of B_a comes into the time window of the Mössbauer measurement and produce relaxation spectra.

The following model, to take into account the dynamics of magnetic exchange interactions, was developed (Fig. 8.52) [19, 157, 158]. For an iron atom in a cluster (=correlated state), the measured effective hyperfine field is the vectorial sum of the applied field B_a and the cluster field B_{cl}. B_{cl} is due to the magnetization of the correlated spins and is caused by the polarization of the electrons of the individual Fe atom, which also depends on the number of nearest neighbours. The clusters are not stable,

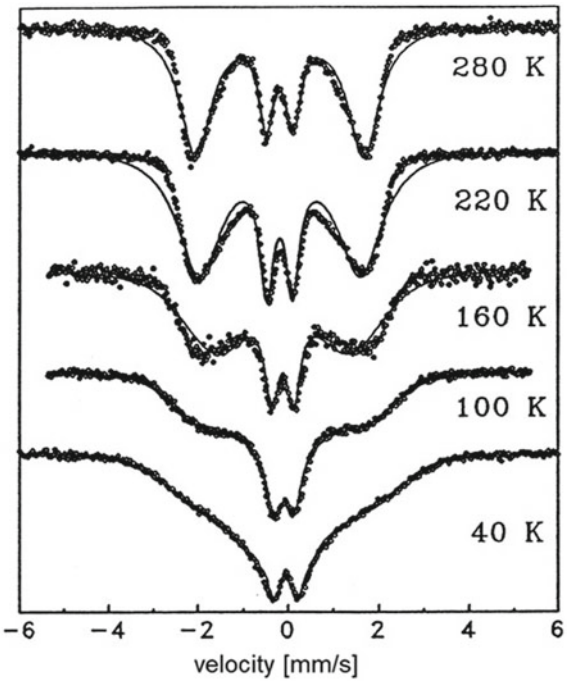

Fig. 8.50 Spectra of $Y(Fe_{0.75}Al_{0.25})_2$ for different temperatures at 13.5 T. Reprinted from [19]

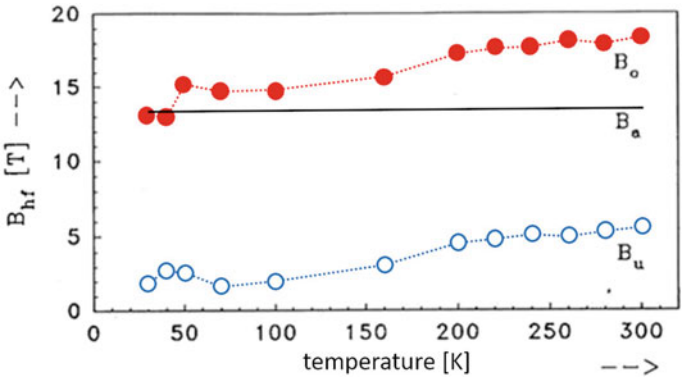

Fig. 8.51 Temperature dependence of flipping fields B_u and B_o at 13.5 T. Reprinted from [19]

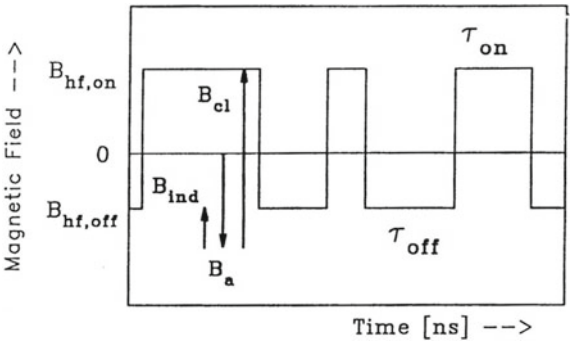

Fig. 8.52 Scheme of the used relaxation model [158].

therefore the correlation persists only for a time interval τ_{on}, afterwards the correlation vanishes. The Fe atom, which is no longer member of a cluster, now senses a hyperfine field $B_a - B_{ind}$. The induced hyperfine field B_{ind} is antiparallel to B_a and is caused by the paramagnetic iron moment. After a time τ_{off} the Fe probe atom changes from uncorrelated state back to a correlated one (Fig. 8.52). This change from correlated to uncorrelated state is a stochastic process, therefore τ_{on} and τ_{off} are average values. The applied field stabilizes the correlation in a way that a stable magnetization appears which produces B_{cl}. The probabilities for the changes are then given by $W_{on\to off} = 1/\tau_{on}$ and $W_{off\to on} = 1/\tau_{off}$. The relaxation time τ which has to be compared with the characteristic time of the Mössbauer effect—the Larmor period of the absorbing Fe nucleus—is given by $1/\tau = 1/\tau_{on} + 1/\tau_{off}$. Beside τ the ratio $a_\tau = \tau_{on}/\tau_{off}$ enters as the second dynamical parameter in the fitting procedure. Because at applied fields higher 4 T the spectra are fully polarized, with vanishing of the 2nd and 5th line, a uniaxial relaxation of the hyperfine fields could be assumed, which can be described by the relaxation equations of Wickman [159, 160]. According to the fact, that due to the crystal structure an electric quadrupole interaction is present, and because measurements are performed on polycrystalline samples, the main axis of the field gradient tensor has an arbitrary orientation in relation to the direction of the applied field. Therefore more sophisticated formula are necessary to describe the relaxation behaviour, as for example developed by Blume [22] and Clauser and Blume [23]. The Hamiltonian in terms of which the nuclear Zeeman and the electrostatic hyperfine interactions can be described is for fields acting at the nucleus which are collinear with the γ-direction, of the form.

$\mathcal{H} = -g_N\mu_N[B_a - B_{ind}\{1 - f(t)\} - B_{cl}f(t)]I_z + \frac{eQV_{\hat{z}\hat{z}}}{4I(2I-1)}\{\frac{1}{2}(3\cos^2\beta - 1)(3I_Z^2 - I^2) + \frac{3}{2}\sin 2\beta[(I_zI_x + I_xI_z)\cos\phi + (I_zI_y + I_yI_z)sin\phi] + \frac{3}{2}\sin^2\beta[(I_x^2 - I_y^2)\cos 2\phi + (I_xI_y + I_yI_x)\sin 2\phi]\}$ where β is the polar and ϕ the azimuth angle between applied field and the largest contribution of the electric field gradient tensor $V_{\hat{z}\hat{z}}$ with respect to the laboratory frame and $f(t)$ denotes a random variable taking the values 0 or 1. In case of only 2 states—correlated or paramagnetic—the size of the relaxation matrix is 16×16, which guarantees short relaxation times. The sign of $eQV_{\hat{z}\hat{z}}$ was determined from measurements in external field 1.5 T at room tem-

perature. Different values for quadrupole splitting, center shift, B_{ind}, and B_{cl} are used for the different Fe environments, whereby the hyperfine fields were assumed to increase with increasing number of Fe atoms in the surrounding. According to the zero-field measurements quadrupole splitting is independent of temperature and centre shift changes only according to second order Doppler shift. These changes were assumed to be the same for all configurations, which means that the Debye temperature does not depend on the local environment. This assumption seems to be reasonable for a metal. Because the quadrupole interaction is much smaller than the magnetic one, in the magnetic split spectra the change in quadrupole splitting has no influence on the shape of the spectra within the given measuring accuracy. Therefore the quadrupole splitting was assumed to be field independent. Line widths are fixed to the values of the calibration α-Fe foil. Asymmetry parameter was set to zero. The number of subspectra and their intensity was fixed by the number of nearest neighbour environments and their probability calculated by binomial distribution. To take into account that an iron atom in a specific surrounding may be part of clusters of different size, two or more subspectra for each surrounding were used. Figure 8.53 gives an example. The spectrum is fitted by five subspectra, each corresponding to a specific surrounding. Each of these subspectra is the sum of two subspectra with different dynamical parameters. The sum intensity of these two subspectra are still fixed to the value obtained from the binomial distribution and the only allowed parameters to change are the two dynamical parameters τ and α_τ. Close to T_f it is necessary to admit an angle θ between B_{cl} and B_a, because in the spin glass regime below T_f the clusters are frozen and applied field is not able to align the inner fields. For simplicity θ was assumed not to change during reestablishment of the correlation. Field and temperature dependence of θ for two concentrations is shown in Fig. 8.54. All measured spectra could be fitted reasonably well within this model. Typical examples are shown in Fig. 8.47. It has to be stressed once more, that the number of subspectra remains the same for zero- and in-field measurements. Thus the distinction between individual iron environments remains. During τ_{off} the iron atom is not part of a correlated region. Therefore it must show paramagnetic behaviour. The field acting on the nucleus during this time B_{ind} is only caused by the moment of the probe atom. In that case paramagnetic behaviour is expected to show a Brillouin-like behaviour, which is really found for all Fe environments (Fig. 8.55). B_{ind} increases with the number of iron neighbours. For temperature $T < \sim T_f$ B_{cl} is antiparallel to the external field B_a. Near T_f the cluster field is not fully aligned, even at the highest field of 13.5 T. The obtained B_{cl} fields decrease with temperature and are only mildy dependent on the Fe concentration x for a given environment (Fig. 8.56). With these two fields a field B_n can be defined by $B_n = (B_{cl}\tau_{on}\cos\theta + B_{ind}\tau_{off})/(\tau_{on} + \tau_{off})$. Because B_n acts on the Fe nucleus, it should be proportional to the macroscopic measured magnetization σ. Since for $Y(Fe_{0.75}Al_{0.25})_2$, as mentioned above, the core contribution is the dominant part of the hyperfine field, B_n should be directly proportional to the bulk magnetization. In the comparison (Fig. 8.57) there is only the hyperfine field constant a free parameter, which turns out to be 11 T/μ_B for all temperatures, in good agreement with values often obtained from standard Mössbauer experiments. This strongly supports the used model. The deviations 4.5 T are due to the fact that because

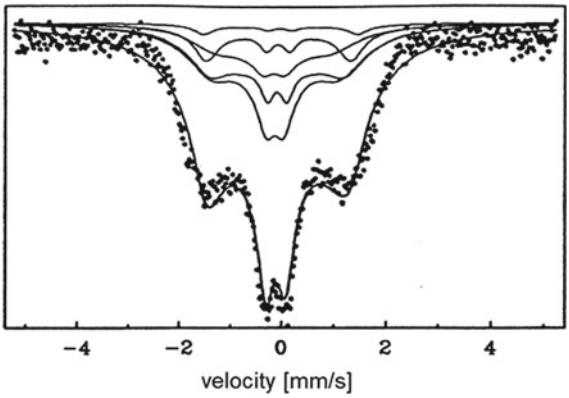

Fig. 8.53 Spectrum of $Y(Fe_{0.75}Al_{0.25})_2$ 100 K and 13.5 T. Subspectra calculated in approximation of fast relaxation. Reprinted from [19]

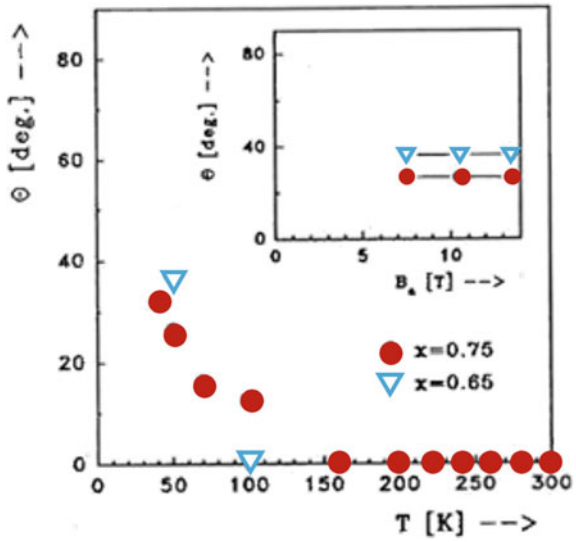

Fig. 8.54 Angle θ in $Y(Fe_xAl_{1-x})_2$ at 13.5 T. Inset: field dependence of θ at 50 K. Reprinted from [19]

of the small splitting of the spectra at low fields the obtained parameters are rather unsure. From the obtained values for τ_{on} and τ_{off} a parameter $p = \tau_{on}/(\tau_{on} + \tau_{off})$ can be calculated, which gives the fraction of time, during which the Fe atom is on average in a correlated state. Hence p also gives the fraction of Fe atoms which are on average at an arbitrary time bound in correlated regions. p increases with field and decreasing temperature for higher field, whereas it starts at lower temperatures to increase (Fig. 8.58). Although nothing can be said from these data about sizes of the correlated regions, the fact that p is about 80% 13.5 T near T_f for $x = 0.75$ shows that the correlated region has to be rather small. p is smaller for lower iron concentrations x for the same field and temperature. Looking now on the relaxation time τ, defined by $1/\tau = 1/\tau_{on} + 1/\tau_{off}$, a common, approximately linear variation with $B_a^{1/2}/t^{3/2}$, with $t = T/T_f$, is found for all investigated samples, at all measuring temperatures

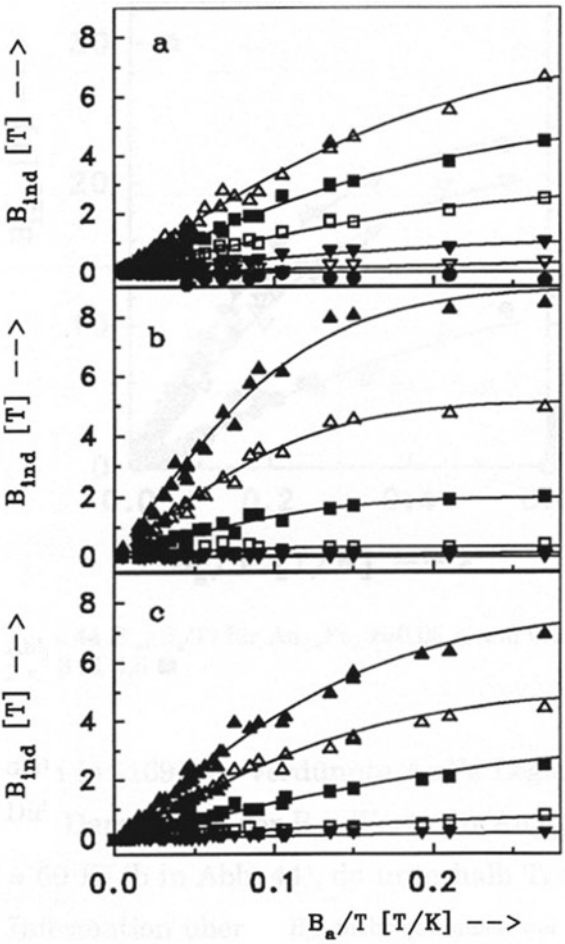

Fig. 8.55 $B_{ind}(B_a/T)$ for $Y(Fe_xAl_{1-x})_2$ $x = 0.40$ (**a**), 0.65 (**b**), and 0.75 (**c**); nearest neighbours Fe: 0 (full circle), 1 (open triangle down), 2 (full triangle down), 3 (open square), 4 (full square), 5 (open triangle up), and 6 (full triangle up). Reprinted from [19]

and all applied fields (Fig. 8.59). In this representation the slope for the higher Fe concentrations is the same, whereas for $x = 0.25$ a less steep increase is found. The analysis of the spectra above approximately $4 \cdot T_f$ was possible with only one set of τ_{on} and τ_{off} values for all different environments. This indicates that at these higher temperatures the expected distribution of correlation times [107, 161–163] are rather narrow. At lower temperatures different times have to be used for different environments, where both τ_{on} and τ_{off} increase with increasing number of iron atoms in the nearest neighbour shell.

The temperature dependence of these times averaged over all surroundings, is very similar for all field values (Fig. 8.60). The increase of $\bar{\tau}_{on}$ with B_a shows that the external field stabilises already existing correlations.

$\bar{\tau}_{off}$, which describes the probability of transition from paramagnetic to correlated state, is practical independent of B_a. That indicates that the applied field stabilizes

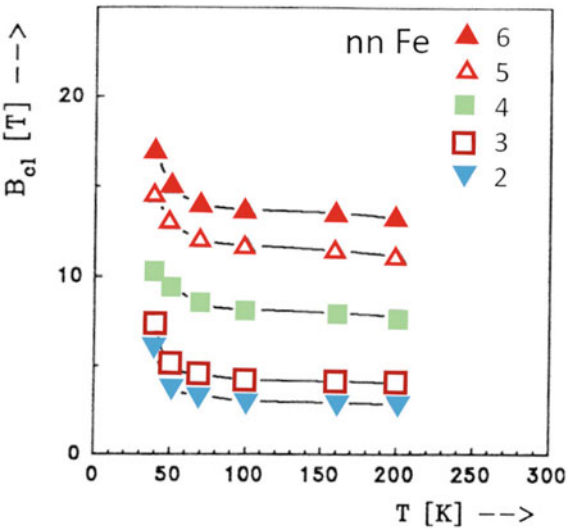

Fig. 8.56 Temperature dependence of cluster field B_{cl} in $Y(Fe_{0.75}Al_{0.25})_2$ at 13.5 T for different Fe surroundings. Reprinted from [19]

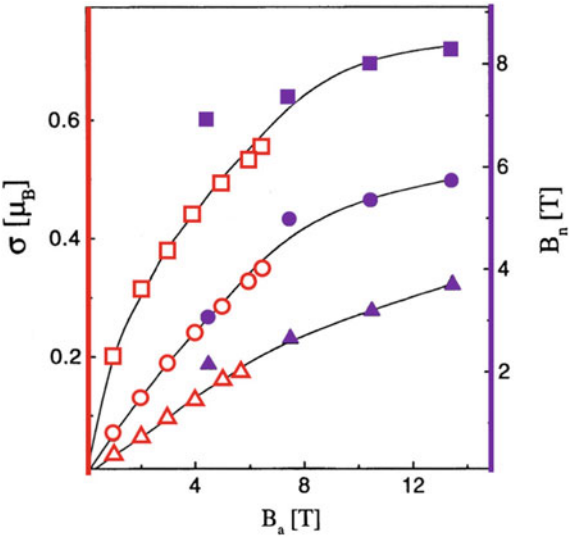

Fig. 8.57 Field dependence of magnetization σ (open symbols) and B_n (full symbols) for $Y(Fe_{0.75}Al_{0.25})_2$ at 50 K (squares), 160 K (circles) and 240 K (triangles). Adapted from [155]

the correlated state but does not support the formation of the clusters. Since the reciprocal values of τ_{on} and τ_{off} are correlated with the probability of formation and/or decay of a correlated region, this implies, following general scaling arguments (e.g. [164, 165]), that larger regions are integrated into the dynamics. Looking on the autocorrelation function, which is proportional to $\bar{\tau}_{on}$, a power law dependence on reduced temperature $t = T/T_f$ is found with an exponent of -2 for the high Fe concentration and -1 for the low Fe concentration (Fig. 8.61). The question why the magnetic correlated regions are not stable after they have formed, but are decaying

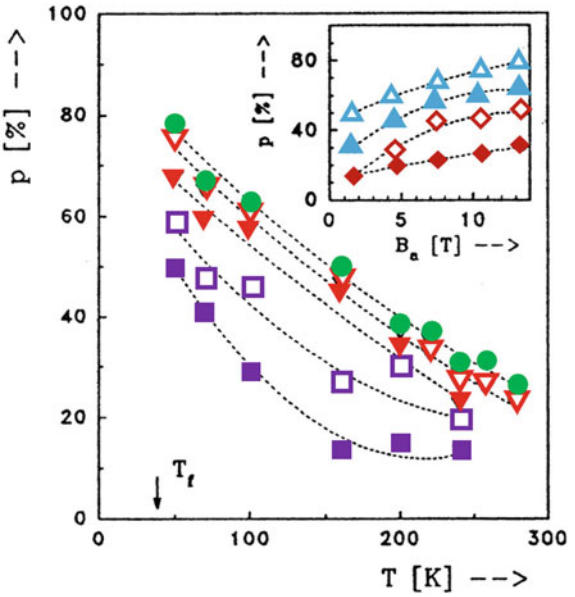

Fig. 8.58 Temperature dependence of the amount of Fe atoms in $Y(Fe_{0.75}Al_{0.25})_2$ in correlated regions at $B_a = 13.5$ T(full circle), 10.5 T (open triangle down), 7.5 T (full triangle down), 4.5 T (open square), and 1.5 T (full square). Inset: field dependence of p for T = 50 K (open triangle up), 100 K (full triangle up), 160 K (open diamond), and 240 K (full diamond). Adapted from [19]

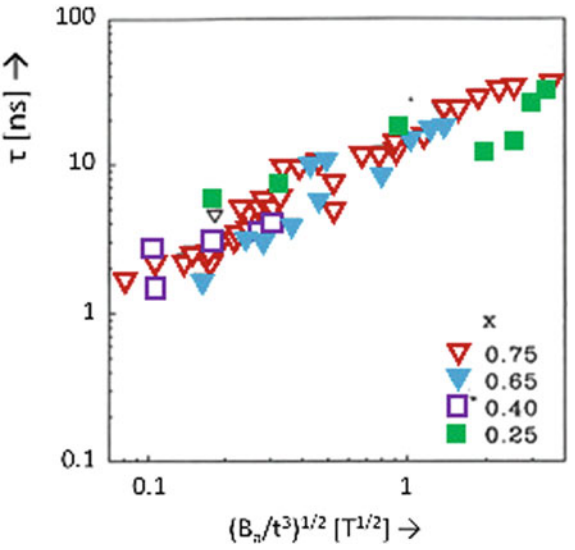

Fig. 8.59 Relaxation time τ in $Y(Fe_xAl_{1-x})_2$ [158]. © IOP Publishing. Reproduced with permission. All rights reserved

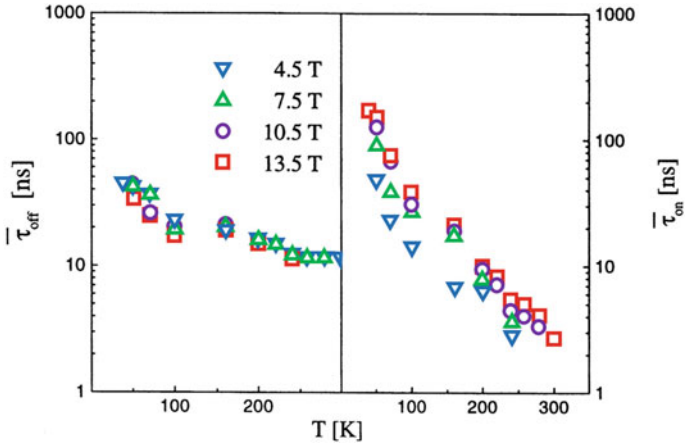

Fig. 8.60 Temperature dependence of $\bar{\tau}_{off}$ (left) and $\bar{\tau}_{on}$ (right) averaged over the different Fe environments for $Y(Fe_{0.75}Al_{0.25})_2$ at different applied fields. Adapted from [154]

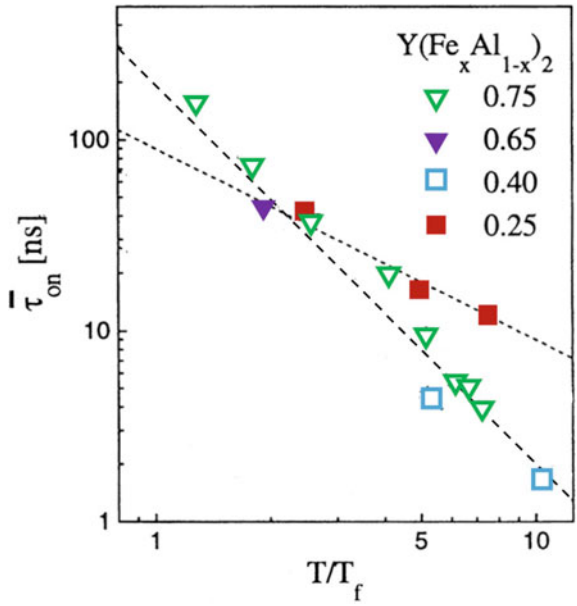

Fig. 8.61 Mean lifetime $\bar{\tau}_{on}$ of the correlated states at 13.5 T as a function of the reduced temperature for the series $Y(Fe_xAl_{1-x})_2$. Adapted from [154]

after a time $\bar{\tau}_{on}$ might be explained by taking into account the influence of entropy (Fig. 8.62). In zero field the energy of a correlated iron atom is lower than the one of an atom in the paramagnetic state due to the exchange interaction of the atom with neighbouring atoms. On the other side the entropy is much lower for an ensemble of correlated iron atoms than for the same number of atoms in the paramagnetic state. If the energy difference between the two states is not large, the entropy cannot be neglected. In an applied field the probability of states being occupied such that the Fe moment is parallel or almost parallel to B_a increases, but all magnetic substates are allowed in paramagnetic atoms and transitions between different spin directions take place so fast that only a resulting B_{ind} is visible in the Mössbauer spectra. The energy of the resulting state is shifted to lower values by $B_a < \mu_{Fe} >$, where $< \mu_{Fe} >$ is the thermal average of the Fe magnetic moment of an uncorrelated Fe atom. For correlated Fe atoms there will be an axial anisotropy inherent in the exchange interaction which permits only parallel or antiparallel orientation of μ_{cl}, like in superparamagnetic systems [166]. The state with direction of the resulting moment μ_{cl} parallel to B_a is shifted by $-\mu_{cl} B_a$ to lower values, and for antiparallel alignment by $+\mu_{cl} B_a$ to higher values. μ_{cl} is the effective magnetic moment of a correlated region. If the magnetic moment of a correlated region changes its direction from close to parallel to close to antiparallel with respect to B_a, the high entropy of the paramagnetic state would favour its occupation, even if the energy of the correlated state was comparable to that of the paramagnetic one (Fig. 8.62). In this picture a decay of correlations is possible. In this model the ratio of the occupation probabilities of the two states can be written as $p_{on}/p_{off} = exp(-\Delta S/k_B + \Delta E/k_B T + \mu_{cl} B_a/k_B T)$, where it is assumed that $\mu_{Fe} << \mu_{cl}$, ΔS is the entropy difference and ΔE is the energy difference of the two states for an Fe atom. The equilibrium condition $p_{on} W_{on\rightarrow off} = p_{off} W_{off\rightarrow on}$ and the definitions of $\tau_{on} = 1/W_{on\rightarrow off}$ and $\tau_{off} = 1/W_{off\rightarrow on}$ give $p_{on}/p_{off} = \tau_{on}/\tau_{off}$. This allows to get information about ΔS, ΔE, and μ_{cl} from the obtained τ_{on}/τ_{off} values. Fits of field and temperature dependence of τ_{on}/τ_{off} are only possible if ΔS, ΔE, and μ_{cl} are assumed to be field and temperature independent (Fig. 8.63). Although fits are not perfect, results of values of ΔS, ΔE, and μ_{cl} should be good enough to get estimation of the order of correct values. The values of ΔS are between 1.3 and 3.2 k_B, the ones of ΔE are between 1×10^{-21} and 1.7×10^{-21} J (corresponding to 72 and 123 K) and those of μ_{cl} are between 6.2 and 8.5 μ_B for all samples. Assuming an Fe moment of 1.77 μ_B as obtained for YFe_2 [63] and parallel alignment of the Fe moments in the correlated regions, gives only three to five Fe atoms per cluster, in good agreement with results of magnetic measurements.

8.6 Conclusion

The presented examples cover a broad range of different magnetic phenomena, investigated in much detail by application of external magnetic fields. In case of Ga substituted Co ferrites it was shown that the magnetically determined weak ferro-

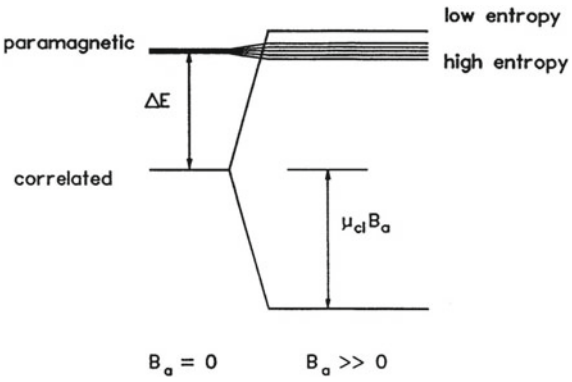

Fig. 8.62 Energy level scheme of the two states which are allowed in the model with and without B_a [158]. © IOP Publishing. Reproduced with permission. All rights reserved

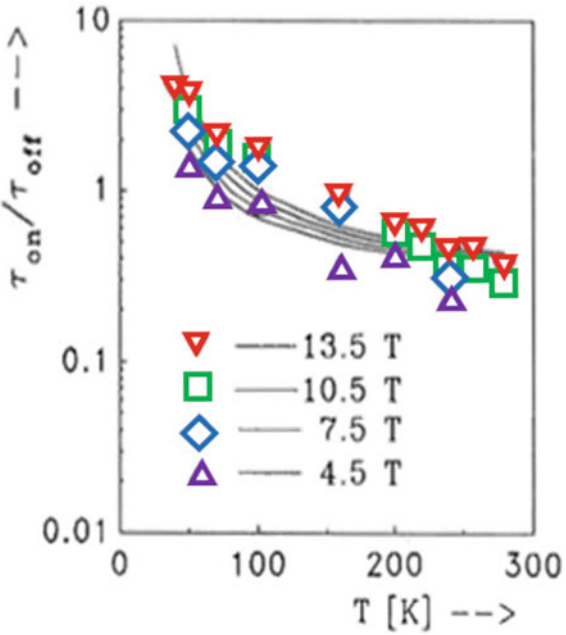

Fig. 8.63 Dependence of τ_{on}/τ_{off} on T for different B_a in $Y(Fe_{0.75}Al_{0.25})_2$ [158]. © IOP Publishing. Reproduced with permission. All rights reserved

magnetism is in fact a ferrimagnet. For $RE_6Fe_{13}X$ compounds the comparison of magnetic investigations with high field Mössbauer results it is shown that even in the highest applied fields the spin moments are canted. In Fe pnictides crystallographically only one Fe site is present, which should lead to only one simple Mössbauer spectrum, which is indeed found in zero field measurements. With the application of an external field, spectra become so complex, that they cannot be explained by only one subspectrum. This is only one example that the external field opens a new window for elucidation of real magnetic ground states, which are not visible without field. In the last example the magnetic behaviour of spin glasses is discussed. After

introduction of the term spin glass, it is shown how very detailed information about local moments, local susceptibilities and magnetic dynamics above the ordering temperature is obtained with help of high field Mössbauer spectroscopy. In all cases it is clear that results of accompanying investigations, as for example detailed structure analysis, are necessary to interpret the results of the Mössbauer measurements correctly. In the ideal case the measurements are accompanied also by theoretical band structure calculations. In that case most information can be gained.

Acknowledgements This chapter reviews some studies accomplished in last decades in the Mössbauer group of the Institute of Solid State Physics, TU Wien, Austria, conducted by its founder Walter Steiner, who initiated these investigations. Some of the work is part of PhD theses of Adrian Pösinger, Joachim Bogner and Robert Ruzitschka. Special thanks goes to Heiner Winkler for his help in extending our program to be able to calculate relaxation spectra. Thanks also to Peter Mohn, Peter Blaha and Karlheinz Schwarz for performing theoretical band structures calculations. Peter Rogl, Andreas Leithe-Jaspers, and Zakir Seidov have prepared some of the discussed samples. Numerous other colleagues and students, who cannot all be mentioned here, have contributed to the presented results.

References

1. S.S. Hanna, J. Heberle, G.J. Perlow, R.S. Preston, D.H. Vincent, Phys. Rev. Lett. **4**(10), 513–515 (1960)
2. J. Chappert, J. de Physique **35**, 12 C6 71–88 (1974)
3. G.L. Whittle, S.J. Campbell, B.D. Maquire, Hyperfine Interactions **15–16**, 661–664 (1983)
4. P. Steiner, D. Gumprecht, W.V. Zdrojewski, S. Hüfner, J. de Physique **35**, C6 523 (1974)
5. W. Gierisch, W. Koch, W. Potzel, F.J. Litterst, P. Steiner, G.M. Kalvius, Hyperfine Interactions **4**, 407–10 (1978)
6. M. Scherg, E.R. Seidel, F.J. Litterst, W. Gierisch, G.M. Kalvius, J. de Physique **35**, C6 527 (1974)
7. S.J. Campbell, P.E. Clark, T.J. Hicks, Sol. Stat. Comm. **24**, 791–792 (1977)
8. J. Chappert, J. Teillet, F. Varret, J. Mag. Mag. Mater. **11**, 200–227 (1979)
9. J. Deportes, B. Kebe, R. Lemaire, J. Mag. Mag. Mater. **54–57**, 1089–1090 (1986)
10. S.M. Fries, C.L. Chien, J. Crummenauer, H.G. Wagner, U. Gonser, Hyperfine Interactions **23**, 273 (1985)
11. R. Coussement, P. Put, G. Scheveneels, F. Hardman, Hyperfine Interactions **23**, 273 (1985)
12. R.E. Watson, A.J. Freeman, Phys. Rev. **123**(6), 2027–2047 (1961)
13. P.W. Anderson, A.M. Clogston, Bull. Amer. Phys. Soc. **6**, 60 (1961)
14. P.W. Anderson, Phys. Rev. **124**, 41 (1961)
15. A. Okiji, J. Kanamori, J. Phys. Soc. Japan **19**(6), 908–915 (1964)
16. J.-M. Greneche, in Mössbauer Spectroscopy eds. Y. Yutaka, G. Lagouche, (Springer, Berlin, Heidelberg, 2013), pp. 187–242
17. C.E. Johnson, M.S. Ridout, T.E. Crawnshaw, Proc. Phys. Soc. **81**, 1079–1090 (1963)
18. W. Marshall, Phys. Rev. **119**(6), pp. 1280–1285
19. A. Pösinger, Dissertation TU Wien (1992)
20. Q.A. Pankhurst, R.J. Pollard, J. Phys. Cond. Matt. **2**, 7329–7337 (1990)
21. S. Dattagupta, Hyperfine Interactions **49**, 253–266 (1989)
22. M. Blume, Phys. Rev. **174**(2), 351–374 (1968)
23. M.J. Clauser, M. Blume, Phys. Rev. B **3**(3), 583–591 (1971)
24. M. Blume, Phys. Rev. B **14**(4), 96–98 (1965)

25. S. Dattagupta, M. Blume, Phys. Rev. B **10**(11), 4540–4550 (1974)
26. M.J. Clauser, Phys. Rev. B **3**(11), 7348–7353 (1971)
27. G.K. Shenoy, B.D. Dunlap, Phys. Rev. B **13**(3), 1353–1356 (1976)
28. M. Blume, J.A. Tjon, Phys. Rev. **165**(2), 446–456 (1968)
29. J.A. Tjon, M. Blume, Phys. Rev. **165**(2), 456–461 (1968)
30. F. Hartmann-Boutron, J. de Physique **37**, 537–556 (1976)
31. C. Chopin, F. Hartmann-Boutron, D. Spanjaard, J. de Physique **37**(12), C6 433–436 (1976)
32. C. Chopin, D. Spanjaard, F. Hartmann-Boutron, J. de Physique **37**(12), C6 73–78 (1976)
33. F. Hartmann-Boutron, Revue Phys. Appl. **18**, 413–430 (1983)
34. F. Hartmann-Boutron, Revue Phys. Appl. **18**, 431–455 (1983)
35. Q.A. Pankhurst, S. Suharan, M.F. Thomas, J. Phys. Cond. Matt. **4**(13), 3551–3558 (1992)
36. B. Window, J. Phys. E **4**, 401–402 (1971)
37. F. Bitter, Rev. Sci. Instr. **7**, 482–488 (1936)
38. C. Otero Arean, J.L. Rodriguez Blanco, J.M. Rubio Gonzales, F. Trobajo, J. Mat. Sci. Letts. **9**, 229 (1990)
39. J.L. Soubeyroux, D. Fiorani, E. Agostinelli, J. Mag. Mag. Mater. **54–57**, 83 (1986)
40. Z. Seidov, G. Sultanov, S. Ibragimov, A. Kaplienko, J. Phys. IV France **7**, C1–265 (1997)
41. M. Reissner, W. Steiner, Z. Seidov, G. Sultanov, Hyperfine Interactions (C) **6**, 193–196 (2002)
42. F. Weitzer, P. Rogl, J. Less-Common Metals **167**, 135 (1990)
43. T. Kajitani, K. Nagayama, T. Umeda, *Proceedings on 12th International Workshop on RE Magnets and their Applications* (Ed. R. Street, Canberra, 1992), pp. 574–583
44. K.G. Knoch, I.R. Harris, Z. Metallk. **83**, 338 (1992)
45. C. Müller, B. Reinsch, G. Petrow, Z. Metallk. **83**, 845–852 12 (1992)
46. H. Klesnar, P. Rogl, J. Mater. Res. **6**, 53 (1991)
47. H. Klesnar, K. Hiebl, P. Rogl, H. Noël, Less-Common Metals **154**, 217 (1989)
48. F. Weitzer, K. Hiebl, Yu. Grin, P. Rogl, H. Noël, J. Appl. Phys. **68**, 3504 (1990)
49. H.S. Li, B.-P. Hu, J.M. Cadogan, J.M.D. Coey, J.P. Gavigan, J. Appl. Phys. **67**, 4841 (1990)
50. P. Schrey, M. Velicescu, J. Mag. Mag. Mater. **101**, 417 (1991)
51. T. Zhao, Ph.D. Thesis, Institute of Metal Research, Shenyang, P.R. China (1995)
52. F. Weitzer, A. Leithe-Jasper, P. Rogl, K. Hiebl, A. Rainbacher, G. Wiesinger, W. Steiner, J. Friedl, F.E. Wagner, J. Appl. Phys. **75**, 7745 (1994)
53. R. Ruzitschka, M. Reissner, W. Steiner, P. Rogl, J. Mag. Mag. Mater. **226–223**, 1443–1445 (2001)
54. G. Wiesinger, A. Rainbacher, W. Steiner, A. Leithe-Jasper, P. Rogl, F. Weitzer, Hyperfine Interactions **94**, 1915–1920 (1994)
55. R. Ruzitschka, M. Reissner, W. Steiner, P. Rogl, J. Mag. Mag. Mater. **242–245**, 806–808 (2002)
56. F. Weitzer, A. Leithe-Jasper, P. Rogl, K. Hiebl, H. Noël, G. Wiesinger, W. Steiner, J. Solid State Chem. **104**, 368 (1993)
57. W. Steiner, R. Haferl, Phys. Stat. Sol. (A) **42**, 739–750 (1977)
58. Q.W. Yan, P.L. Zhang, X.D. Sun, B.P. Hu, Y.Z. Wang, X.L. Rao, G.C. Liu, C. Gou, D.F. Chen, Y.F. Cheng, J. Phys, Cond. Matt. **6**, 3101 (1994)
59. F. Wang, B.-G. Shen, H. Gong, X.D. Sun, P. Zhang, Q. Yan, J. Mag. Mag. Mater. **177–181**, 1056 (1998)
60. P. Schobinger-Papamantellos, K.H.J. Buschow, C.H. de Groot, F.R. de Boer, C. Ritter, F. Fauth, G. Boettger, J. Alloys Comp. **280**, 44 (1998)
61. P. Schobinger-Papamantellos, K.H.J. Buschow, C.H. de Groot, F.R. de Boer, G. Boettger, C. Ritter, J. Phys, Cond. Matt. **11**, 4459 (1999)
62. P. Schobinger-Papamantellos, K.H.J. Buschow, C.H. de Groot, F.R. de Boer, C. Ritter, J. Mag. Mag. Mater. **218**, 31 (2000)
63. C. Ritter, J. Phys, Cond. Matt. **1**, 2765 (1989)
64. I. Oftedal, Z. Kristllogr, A **66**, 517 (1928)
65. W. Jeitschko W, D.J. Braun, Acta Crystallogr. B **33**, 3401 (1977)
66. T.M. Tritt, *Recent Trends in Thermoelectric Materials I* (Academia Press, New York, 2001)

67. B.C. Sales, Filled skutterudites, in *Handbook on the Physics and Chemistry of Rare Earths*, vol. 33, ed. by K.A. Gschneidner Jr., J.C.G. Buenzli, V.K. Pecharsky (Elsevier Science, Amsterdam, 2003), pp. 1–34
68. T. Cichorek, A.C. Mota, F. Steglich, N.A. Frederick, W.M. Yuhasz, M.B. Maple, Phys. Rev. Lett. **94**, 107002 (2005)
69. M.B. Maple, E.D. Bauer, N.A. Frederick, P.C. Ho, W.M. Yuhasz, V.S. Zapf, Physica B **338**, 29–33 (2003)
70. C. Uher, Skutterudites prospective novel thermoelectrics, in *Recent Trends in Thermoelectric Materials Reserach I, Semiconductors and Semimetals 69, 139–253*, ed. by T.M. Tritt (Academic, New York, 2001)
71. G.A. Slack, *CRC Handbook of Thermoelectrics 1994*, ed. by D.M. Rowe (CRC Press, Boca Rator, FL, 1995), pp. 407–440
72. I. Shirotani, K. Ohno, C. Sekine, T. Yagi, T. Kawakami, T. Nakanishi, H. Takahashi, J. Tang, A. Matsushita, T. Matsumoto, Physica B **281–282**, 1021 (2000)
73. N. Takeda, M. Ishikawa, J. Phys. Soc. Jpn. **69**, 868 (2000)
74. I. Shirotani, T. Uchiumi, K. Ohno, C. Sekine, Y. Nakazawa, K. Kanoda, S. Todo, T. Yagi, Phys. Rev. B **56**, 7866 (1997)
75. C. Sekine, T. Uchiumi, I. Shirotani, T. Yagi, Phys. Rev. Lett. **79**, 3218 (1997)
76. M.E. Danebrock, C.B.H. Evers, W. Jeitschko, J. Phys. Chem. Solids **57**, 381 (1996)
77. E. Bauer, St. Berger, A. Galatanu, M. Galli, H. Michor, G. Hilscher, Ch. Paul, B. Ni, M.M. Abd-Elmeguid, V.H. Tran, A. Grytsiv, P. Rogl, Phys. Rev. B **63**, 224414 (2001)
78. N.R. Dilley, E.J. Freeman, E.D. Bauer, M.B. Maple, Phys. Rev. B **58**, 6287 (1998)
79. N. Takeda, M. Ishikawa, J. Phys. Cond. Matt. **13**, 5971 (2001)
80. E. Bauer, A. Galatanu, H. Michor, G. Hilscher, P. Rogl, P. Boulet, H. Noël, Eur. Phys. J. B **14**, 483 (2000)
81. A. Grytsiv, P. Rogl, St. Berger, Ch. Paul, E. Bauer, C. Godart, B. Ni, M.M. Abd-Elmegiud, A. Saccone, R. Ferro, D. Kaczorowski, Phys. Rev. B **66**, 094411 (2002)
82. A. Leithe-Jasper, W. Schnelle, H. Rosner, M. Baenitz, A. Rabis, A.A. Gippius, E.N. Morozova, H. Borrmann, U. Burkhardt, R. Ramlau, U. Schwarz, J.A. Mydosh, Yu. Grin, V. Ksenofontov, S. Reiman, Phys. Rev. B **70**, 214418 (2004)
83. A. Leithe-Jasper, W. Schnelle, H. Rosner, R. Cardoso-Gil, M. Baenitz, J.A. Mydosh, Yu. Grin, M. Reissner, W. Steiner, Phys. Rev. B **77**, 064412 (2008)
84. E. Bauer, St. Berger, Ch. Paul, M. Della Mea, G. Hilscher G, H. Michor, M. Reissner, W. Steiner, A. Grytsiv, P. Rogl, E.W. Scheidt, Phys. Rev. B **66**, 214421 (2002)
85. M.S. Torikachvili, J.W. Chen, Y. Dalichaouch, R.P. Guertin, M.W. McElfresh, C. Rossel, M.B. Maple, G.P. Meisner, Phys. Rev. B **36**, 8660 (1987)
86. Y. Aoki, T. Namiki, T.D. Matsuda, K. Abe, H. Sugawara, H. Sato, Phys. Rev. B **65**, 064446 (2002)
87. Y. Nakamishi, T. Simizu, M. Yoshizawa, T. Matsuda, H. Sugawara, H. Sato, Phys. Rev. B **63**, 184429 (2001)
88. P. Meisner, Physica **108B**, 763 (1981)
89. D.J. Singh, I.I. Mazin, Phys. Rev. B **56**, R1650–3 (1997)
90. K. Takegahara, H. Harima, J. Phys. Soc. Jpn. **71**(Suppl.) 240–242 (2002)
91. K. Tanaka, Y. Kawahito, Y. Yonezawa, Y. Kikuchi, H. Aoki, K. Kuwahara, M. Ichihara, H. Sugawara, Y. Aoki, H. Sato, J. Phys. Soc. Jpn. **76**, 103704 (2007)
92. M. Reissner, E. Bauer, W. Steiner, P. Rogl, J. Mag. Mag. Mater. **272–276**, 813 (2004)
93. G.K. Shenoy, D.R. Noakes, G.P. Meisner, J. Appl. Phys. **53**, 2628–2630 (1982)
94. M. Reissner, E. Bauer, W. Steiner, P. Rogl, A. Leithe-Jasper, Y. Grin, Hyperfine Interactions **182**, 15–22 (2008)
95. A. Leithe-Jasper, D. Kaczorowski, P. Rogl, J. Bogner, M. Reissner, W. Steiner, G. Wiesinger, C. Godart, Sol. Stat. Comm. **109**, 395–400 (1999)
96. G.J. Long, B. Mathieu, B.C. Sales, R.P. Hermann, F. Grandjean, J. Appl. Phys. **92**, 7236–7241 (2002)
97. P. Blaha, Private communication

98. P. Mohn, Private communication
99. P. Ghosez, M. Veithen, J. Phys. Cond. Matt. **19**, 096002 (2007)
100. G.J. Long, D. Hautot, F. Grandjean, D.T. Morelli, G.P. Meisner, Phys. Rev. B **60**, 7410–7418 (1999)
101. G.P. Meisner, D.T. Morelli, S. Hu, J. Yang, C. Uher, Phys. Rev. Lett. **80**, 3551–3554 (1998)
102. V. Cannella, J.A. Mydosh, Phys. Rev. B **6**(11), 4220 (1972)
103. P.J. Ford, Contemp. Phys. **23**(2), 141–168 (1982)
104. K. Binder, A.P. Young, Rev. Mod. Phys. **58**, 801–976 (1986)
105. D. Chowdhury, *Spin Glasses and Other Frustrated Systems* (World Scientific, Singapore, 1986)
106. J.A. Mydosh, G.J. Nieuwenhuys, Dilute transition metal alloys; spin glasses in *Ferromagnetic Materials*, vol. 1 ed. by E.P. Wohlfarth (1980)
107. J.A. Mydosh, *Spin Glasses: An Experimental Introduction* (Taylor and Francis, 1993)
108. N. Rivier, Wiss. Z., Techn. Univ. Dresden (1974)
109. M.A. Rudermann, C. Kittel, Phys. Rev. **96**, 99 (1954)
110. T. Kasuya, Prog. Theor. Phys. **16**, 45 (1956)
111. K. Yosida, Phys. Rev. **106**, 893 (1957)
112. K. Yosida, Phys. Rev. **107**, 396 (1957)
113. G. Toulouse, Comm. Phys. **2**, 115–119 (1977)
114. G. Toulouse, Lect. Notes Phys. **192**, 2–17 (1983)
115. B.R. Coles, B.V. Sarkissian, R.H. Taylor, Phil. Mag. B **37**, 489 (1987)
116. P.A. Beck, Met. Trans. **2**, 2015 (1971)
117. P.A. Beck, J. Less-Common Met. **28**, 193 (1972)
118. R.W. Tustion, P.A. Beck, Sol. Stat. Comm. **21**, 517 (1977)
119. C.N. Guy, J. Phys. F **5**, L242 (1975)
120. C.N. Guy, Physica 86-88B, 877 (1977)
121. C.N. Guy, J. Phys. F **7**, 1505 (1977)
122. C.N. Guy, J. Phys. F **8**(6), 1305–19 (1978)
123. M. Reissner, W. Steiner, J.P. Kappler, P. Bauer, M.J. Besnus, J. Phys. F Met. Phys. **14**, 1249–1259 (1984)
124. L.E. Wenger, P.H. Keesorn, Phys. Rev. B **11**, 3497 (1975)
125. R.J. Borg, R. Booth, C.E. Violet, Phys. Rev. Lett. **11**, 464 (1963)
126. V. Gonser, V.W. Grant, C.J. Meecham, A.M. Muir, H. Wiedersich, J. Appl. Phys. **36**, 2124 (1965)
127. P.P. Craig, W.A. Steyert, Phys. Rev. Lett. **13**, 802 (1964)
128. C.E. Violet, R.J. Borg, Phys. Rev. **149**, 540 (1966)
129. A.P. Murani, J. Mag. Mag. Mat. **5**, 95 (1977)
130. A.P. Murani, J. Appl. Phys. **49**, 1604 (1978)
131. A.P. Murani, J.L. Tholence, Sol. Stat. Comm. **22**, 25 (1977)
132. S.F. Edwards, P.W. Anderson, J. Phys. F **5**, 965 (1975)
133. D. Sherrington, S. Kirkpatrick, Phys. Rev. Lett. **35**(26), 1792–6 (1975)
134. C.M. Soukoulis, G.S. Grest, K. Levin, Phys. Rev. Lett. **41**, 568 (1978)
135. G. Parisi, G. Toulouse, J. Physique Lett. **41**, L361 (1980)
136. J.L. Tholence, R. Tournier, J. Physique 35, C4 229 (1974)
137. E.P. Wohlfarth, Physica 86-88B, 852–853 (1977)
138. H. Yamada, J. Inoue, K. Terao, S. Kanada, M. Shimizu, J. Phys. F Met. Phys. **14**, 1943 (1984)
139. E. Burzo, Z. Angew, Phys. **32**, 127–132 (1971)
140. E. Burzo, Phys. Rev. B **17**, 1414–1423 (1978)
141. M. Reissner, W. Steiner, Hyperfine Interactions **28**, 1017–1020 (1986)
142. J.M. Preston, J.R. Stewart, M. Reissner, W. Steiner, R. Cywinski, Appl. Phys. A **74**, S689–S691 (2002)
143. M. Reissner, Thesis TU-Wien (1990)
144. M. Aoki, H. Yamada, J. Magn. Magn. Mater. **78**, 377 (1989)
145. M. Aoki, H. Yamada, Sol. Stat. Comm. **72**, 21 (1981)

146. C. Rizzuto, Rep. Prog. Phys. **37**, 147 (1974)
147. G. Grüner, Adv. Phys. **23**, 941 (1974)
148. J. Deuz, P.H. Dederichs, R. Zeller, J. Phys. F Met. Phys. **11**, 1787 (1981)
149. O. Eriksson, A. Svane, J. Phys. Cond. Matt. **1**, 1589 (1989)
150. A. Pösinger, M. Reissner, W. Steiner, P. Blaha, P. Mohn, K. Schwarz, J. Phys. Cond. Matt. **5**, 7277–7288 (1993)
151. I. Vincze, J. Balogh, Z. Foris, D. Kaptas, T. Kemeny, Sol. Stat. Comm. **77**, 757 (1991)
152. C. Meyer, F. Hartmann-Boutron, Hyperfine Interactions **59**, 219 (1990)
153. Y. Furukawa, Y. Nakai, N. Kunitoni, J. Phys. Soc. Jpn. **59**, 2237 (1990)
154. J. Bogner, H. Schachner, M. Reissner, W. Steiner, Aust. J. Phys. **51**(2), 349–362 (1998)
155. W. Steiner, M. Reissner, A. Pösinger, H. Winkler, A.X. Trautwein, Proc. XXX Zakopane School Physica **185–195** (1995)
156. A. Pösinger, M. Reissner, W. Steiner, Physica B **155**, 211–214 (1989)
157. A. Pösinger, H. Winkler, W. Steiner, A.X. Trautwein, M. Reissner, J. Phys. Cond. Matt. **3**, 2713 (1991)
158. A. Pösinger, H. Winkler, W. Steiner, A.X. Trautwein, M. Reissner, J. Phys. C **5**, 3653 (1993)
159. H.H. Wickman, *Mössbauer Paramagnetic Hyperfine Structure in Mössbauer effect Methodology*, vol. 2, ed. by I.J. Gruverman (Plenum Press, New York, 1966), pp. S39–S66
160. H.H. Wickman, M.P. Klein, D.A. Shirley, Phys. Rev. **152**, 345 (1966)
161. A.P. Murani, J. Mag. Mag. Mater. **22**, 271 (1981)
162. Y.J. Uemura, T. Yamazaki, D.R. Harshman, M. Senba, E.J. Ansaldo, Phys. Rev. B **31**, 546 (1985)
163. I.A. Campbell, A. Amato, F.N. Gygax, D. Herlach, A. Schenk, R. Cywinski, S.H. Kilcoyne, Phys. Rev. Lett. **72**, 12 (1994)
164. A.T. Ogielsky, Phys. Rev. B **32**, 7384 (1985)
165. H. Rieger, *Annual Review of Computational Physics*, vol. II, ed. by D. Stauffer (World Scientific, Singapore, 1995), p. 295
166. L. Néel, Phil. Mag. Suppl. **4**, 191 (1955)